ACES Asian Chemical Editorial Society
doi.org/10.1002/asia.202200591
CHEMISTRY AN ASIAN JOURNAL Review
www.chemasianj.org

DNA Origami in the Quest for Membrane Piercing

Naresh Niranjan Dhanasekar[+],*[a] Durairaj Thiyagarajan,[b] and Dhiraj Bhatia[c]

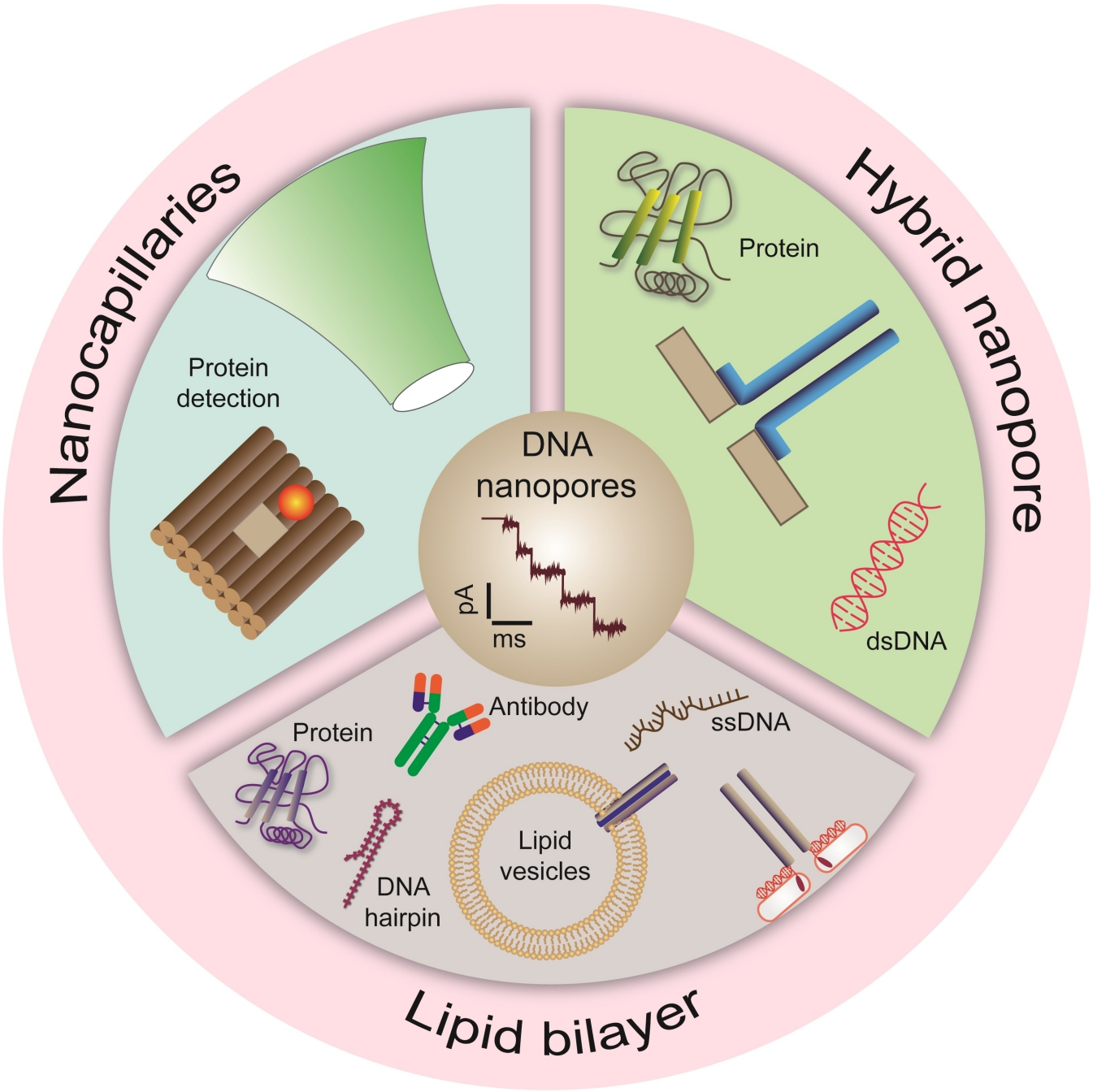

Abstract: The tool kit for label-free single-molecule sensing, nucleic acid sequencing (DNA, RNA and protein) and other biotechnological applications has been significantly broadened due to the wide range of available nanopore-based technologies. Currently, various sources of nanopores, including biological, fabricated solid-state, hybrid and recently *de novo* chemically synthesized ion-like channels have put in use for rapid single-molecule sensing of biomolecules and other diagnostic applications. At length scales of hundreds of nanometers, DNA nanotechnology, particularly DNA origami-based devices, enables the assembly of complex and dynamic 3-dimensional nanostructures, including nanopores with precise control over the size/shape. DNA origami technology has enabled to construct nanopores by DNA alone or hybrid architects with solid-state nanopore devices or nanocapillaries. In this review, we briefly discuss the nanopore technique that uses DNA nanotechnology to construct such individual pores in lipid-based systems or coupled with other solid-state devices, nanocapillaries for enhanced biosensing function. We summarize various DNA-based design nanopores and explore the sensing properties of such DNA channels. Apart from DNA origami channels we also pointed the design principles of RNA nanopores for peptide sensing applications.

1. Introduction

Transport of small molecules across membranes occurs through nanometer sized protein/ion channels forming the fundamental aspects of biology.[1] Most of these are naturally occurring or protein-based, allowing molecules including ions, to move in- and out of the cell. Nanopore-based channels are a relatively new technique for detecting single-molecules in solution and are garnering popularity due to their wide spread biomedical applications including DNA sequencing,[2,3] peptide fingerprinting,[4–6] antigen detection[7] and disease diagnostics.[8] Nanopore sensing employs the single-molecule technique of resistive pulsing[9] which offers highly precise identification of analytes in an aqueous environment.[10–12] A nanopore is typically a nanometer sized (1–100 nm in diameter) cavity in the insulating membrane partitioned between the two chambers (*cis* or *trans*), with the chambers filled with conductive solution (e.g., 1 M KCl). The flow of ions through the open pore is measured by the application of electric potential. However, when an analyte (biomolecule) bind or translocate from one end to the other, which is influenced by the electric field, it partially blocks the open current, contributing to the sensitivity of the nanopore in biosensing.[13,14]

Initially, biological protein systems drew the attention of nanopore scientists as a potential weapon capable of spontaneously inserting into synthetic lipid bilayers. One such biological channel, α-hemolysin, has been extensively modified for single-molecule sensing for various analytes, including nucleic acid.[15] Utilizing this principle, Oxford Nanopore has developed a nanopore-based device for DNA sequencing that incorporates such membrane protein pores into a nano-sized chip.[16,17] The key advantages of biological nanopores are their ability to be chemically and genetically modified, remain stable (open current) for longer hours in membranes, their ease of production, cost effectiveness, integration into microfluidics and other nano-based systems.[18] Although well qualified for single analyte detection, fixed pore size/shape and unpredictability in response to environmental conditions (high temperature and pH) limit the use of biological nanopore systems for larger molecules such as folded proteins, dsDNA and other complex enzymes.[19,20]

To address these issues, solid-state nanopore systems were introduced in 2001.[21] Solid-state nanopores are constructed by drilling a hole into synthetic material, primarily silicon nitride (SiN), using focused ion-beam or dielectric-break down.[22] In contrast to biological nanopore system solid-state devices are simple to manipulate, allowing easy tuning of pore size and shape[23] as well as chemical modification (e.g., lipid or polymer)[24,25] via various surface chemistry ideologies. Additionally, glass nanocapillaries were also used as a functional material for generating nanopores.[26,27] Despite its potential applications, it is still grueling for the solid-state nanopore systems to attain such high accuracy and precision. Although inspired by protein nanopores, the metallic nanopores frequently produce gating signals that cause no difference from the analyte. Further, to study protein nanopores in the lipid free environment and to further develop the sequencing system, Hall and colleagues introduced the concept of hybrid nanopore for the first time in 2010.[28] These nanopores were created by inserting a protein nanopore into a solid-state nanopore system. However, controlling protein insertion and orientation was a major challenge that Cressoit *et al.*[29] overcame and the created hybrid nanopores have potential applications in sensing various biomolecules such as protein, peptides and nucleic acids. Thus, hybrid nanopores can functionalize previously unfunctionalized solid-state nanopores by leveraging the excellent functionality of biomolecules. It is clear from the preceding discussion that both biological and solid-state nanopores are versatile tools for molecular biosensing, but each approach has its own limitations. Thus, new tools are required

[a] *Dr. N. Niranjan Dhanasekar*[+]
Department of Chemical and Biomolecular Engineering,
Johns Hopkins University,
Baltimore, MD 21218 (USA)
E-mail: ndhanas1@jhu.edu
nareshnila@gmail.com

[b] *Dr. D. Thiyagarajan*
Helmholtz Institute for Pharmaceutical Research,
Helmholtz Center for Infection Research,
Saarbrücken 66123 (Germany)

[c] *Prof. D. Bhatia*
Biological Engineering Discipline,
Indian Institute of Technology Gandhinagar,
382355, Gujarat (India)

[+] *Present address: No. 80/12, Avadi Srinivasan Street, Choolai, Chennai – 600112, Tamil Nadu (India)*

to create more amenable and stable nanopores, which could enable more specific, robust and versatile sensing using nanopore-based platforms.

One possible approach is to use customized nanopores, which have recently gained tremendous reputation due to their self-assembled properties. DNA-based nanotechnology[30,31] is the ideal technique which allows to fabricate a wide range nanosized objects with precise geometry and surface properties.[32,33] The created DNA nano constructs serve for its wide range of applications such as nanophotonics,[34] nanoelectronics (nanorobots),[35,36] plasmonics,[37] super-resolution microscopy imaging[38,39] and life-science based applications such as drug-delivery,[40–42] tissue engineering,[43] biosensing,[10,11,44–46] cancer therapy[47,48] and diseases diagnostics.[49–51] Because of their ability to precisely engineer their properties, particularly shape, confinement and function, these nano constructs are very appealing in nanopore sensing applications. The caliber of such synthetic DNA nanostructures to form pore-like properties in synthetic bilayers mimics the action of biological protein channels. We enlighten the readers in this review by demonstrating how these small moveable DNA nanostructures have benefited the field of nanopore science. We begin with presenting how these rigid DNA-based nanostructures were used alone to form membrane-based protein-like channels and their role in single-molecule analyte detection. Later, we show how these nanostructures could be used to benefit other existing nanopores such as solid-state devices and capillary-based nanopore techniques.

Naresh Niranjan Dhanasekar obtained his PhD from Jacobs University Bremen, Germany in the area of Biochemistry (Bacterial membrane protein channels). He moved to Johns Hopkins University, USA in 2017 for his Post-Doctoral Program to work in the area of DNA origami nanopores. His research interest includes protein nanopores and synthetic DNA origami channels.

Durairaj Thiyagarajan received his PhD in Biosciences and Bioengineering discipline from Indian Institute of Technology Guwahati, India. He moved to Helmholtz Center for Infection Research, Germany for his Post-Doctoral program where he is currently involved in nanodrug delivery towards lung infections. His research interests include antimicrobial resistance, antibiofilm agents, nucleic acid delivery and lung therapeutics including antimicrobial nanomaterials and vaccine candidates.

Dhiraj completed his PhD research at NCBS TIFR in Bangalore, India in DNA Nanotechnology. Post PhD he went to Curie Institute in Paris to join the team of Ludger Johannes initially as a Curie fellow and later as an HFSP long-term fellow, where he learnt the cellular and biological applications of DNA nanodevices. In 2018, he moved to India to start his own laboratory at Indian Institute of Technology, Gandhi nagar where he is an Assistant Professor and Ramanujan fellow. His lab focusses on translational aspects of DNA nanotechnology to develop tools to program biological systems having biomedical applications.

2. Nucleic acid (DNA and RNA) based protein-like synthetic nanochannels

2.1. DNA nanopores in lipid vesicles/lipid bilayer

2.1.1. Cholesterol based DNA origami channels

The entropicity associated with inserting synthetic pores into the hydrophobic core of lipid membranes makes designing membrane-penetrating nanopores that can function as protein-like channels extremely challenging. Despite the difficulties associated with such design schemes, many synthetic constructs made from peptides, proteins, chemical compounds and DNA have received significant attention in the field of biosensing and other life-science based applications. Because of the modular nature of DNA designs, membrane anchors can be attached in the desired location and easily penetrated into organic lipid or other lipid-free bilayer systems.[28,29] Inspired, from the DNA sequencing protein channel, α-hemolysin, Langecker and colleagues first constructed the biomimetic DNA nanopore using the design principles of DNA origami nanotechnology.[31] The 2 nm-diameter DNA origami nanochannel consists of a stem region made of 54-helix bundle (HB) that aids in membrane penetration and a branched cap-like structure decorated with 26-cholesterol anchors that adheres to membrane's *cis* side (Table 1 and Figure 1A). The assembly was confirmed by transmission electron microscopy (TEM), which shows a clean puncturing of the nanostructures in 1-palmitoyl-2-oleoyl-glycero-3-phosphocholine (POPC) vesicles in perpendicular direction. The pore-forming tendency of the assembled DNA nanochannel is further confirmed from electrophysiology measurements. On applying a positive transmembrane potential of +200 mV, they formed clean channels in 1,2-diphytanoyl-*sn*-glycero-3-phosphocholine (DPhPC) bilayers with long lived single-channel ohmic conductance ranging between 0.72 and 1.02 nS in 1 M KCl, pH 8.0. Some of these DNA nanopores exhibited gating like behavior that varied with the applied transmembrane potential. They also built mutant channels with lengths of 15 and 14 nm that differed in the sequence of the DNA stem portion. The wild-type construct channel exhibited only a single population of cells with a longer gating time period of 10.5 ms, whereas, the mutant channels had two distinct populations with a shorter gating time frequencies of

Table 1. DNA origami nanostructures containing their respective hydrophobic anchors in lipid membranes.

S. No	Origami type	Type and no. of membrane anchors	Bilayer type/lipid	Buffer concentration/pH	Conductance	Applications
1.	Stem and cap model[10]	Cholesterol/26	Orbit-16 device Planar lipid bilayer (DPhPC)	1 M KCl, 2 mM $MgCl_2$, 10 mm Tris and 1 mM EDTA, pH 8.0	0.87 ± 0.15 nS	DNA hairpin and quadruplex translocation
2.	DNA nanotube[102]	Ethyl chemistry	Orbit-16 device Planar lipid bilayer (DPhPC)	0.3 M KCl 1 M KCl Buffered with 10 mM HEPES, pH 8.0	0.6 nS 1.1 nS	–
3.	DNA 6-helix bundle[70,71]	Ethyl-PPT/72	Orbit-16 device Planar lipid bilayer (DPhPC)	1 M KCl, 50 mM Tris, pH 5.0	0.39 ± 0.09 nS	Cytotoxicity studies
4.	DNA nanobarrel[11]	Cholesterol/24	Orbit-16 device Planar lipid bilayer (DPhPC)	1 M KCl, 10 mM HEPES, pH 8.0	2.37 ± 0.30 nS	Protein translocation
5.	Nanocylinder from DNA tile[90]	Cholesterol/2-4	Lipid capillary nanobilayer (DPhPC)	1 M KCl, 10 mM MES, pH 6.0	0.15–0.30 nS	–
6.	DNA barrel[32]	Cholesterol/19	Planar lipid bilayer (DPhPC)	1 M KCl, 10 mM MES, pH 6.0	30–40 nS	–
7.	RNA origami cylinder[88]	Cholesterol/2-3	Planar lipid bilayer (DPhPC)	1 M KCl, 5 mM HEPES, pH 8	3–4 nS	Poly arginine sensing
8.	Pin, wheel and T-like DNA channel[54]	Tocopherol/26 Tocopherol/57 Biotinylated lipid conjugation	Droplet-interface bilayer (DPhPC)	1 M KCl and 5 mM $MgCl_2$	Pin: 1.6 nS (rarely inserted) Wheel: 1.5 nS (frequent) T-channel: 3.1 ± 0.3 nS (strong and frequent)	DNA translocation
9.	Single duplex DNA channel[75]	Porphyrin/6	Planar lipid bilayer (DPhPC)	1 M KCl, 10 mM MES, pH 6.0.	0.06–0.08 nS	–
10.	DNA nanocylinder[56]	TPP/2	Orbit-16 device Planar lipid bilayer (DPhPC)	1 M KCl, 10 mM HEPES, pH 8	1.62 ± 0.07 nS	–
11.	DNA origami plate (square)[64]	Cholesterol/64	Orbit Mini device (DPhPC)	1 M KCl, 10 mM HEPES, pH 7.6	Plate with no lid: 2.51 ± 0.35 nS; 5.92 ± 0.43 nS; Plate with closed lid: 0.64 ± 0.10 nS Plate with open lid: 2.31 ± 0.18 nS	Trypsin and green fluorescent protein translocation
12.	Nanopore formed from subunit assembly[65]	Cholesterol	Orbit Mini device Planar lipid bilayer (DPhPC)	1 M KCl, 10 mM HEPES, pH 7.4	Pre-assembled nanopore: 0.70 ± 0.27 nS Pore assembly by DNA trigger: 0.69 ± 0.12 nS	Sulforhodamine B and Ca^{2+} transport through vesicles
13.	DNA cap and barrel[66]	Cholesterol	Orbit Mini and Orbit 16 Planar lipid bilayer (DPhPC)	1 M KCl, 10 mM HEPES, pH 7.4	Triangle-10: 2.10 ± 0.21 nS; Square-10: 4.58 ± 0.27 nS; Square-20: 8.91 ± 0.33 nS	IgG sensing Human SARS-CoV-2 antibodies detection

DPhPC: 1,2-diphytanoyl-*sn*-glycero-3-phosphocholine; EDTA: Ethylene diamine tetraacetic acid; Ethyl-PPT: Ethyl-phosphorothioates; HEPES: 4-(2-hydroxyethyl)-1-piperazine ethane sulfonic acid; MES: 2-(*N*-morpholino) ethane sulfonic acid; SARS-CoV-2: Severe acute respiratory syndrome coronavirus 2; TPP: Acetylene-tetraphenyl porphyrin; Tris: Tris (hydroxymethyl) aminomethane.

1.3 and 9.2 ms, respectively. Additionally, sensing experiments revealed that the syringe-like DNA channel was capable of transporting both DNA hairpins and quadruplex molecules (Figure 1B).[10]

Biological channels such as porins[52] and other ion channels are usually untainted by the bilayer systems.[53] However, synthetic channels, like DNA nanopores, are exceedingly flexible, leaky and their efficacy is also dependent on the bilayer systems.[54,55] Thus, channel conductance queries in accordance with channel geometry/type of bilayer systems remain unclear for DNA channels. By using the PEG polymer, the aforesaid challenges were solved experimentally,[56] which they had previously used to figure out the size of many protein channels.[57] Electrophysiology measurements with PEG molecules (size PEG_{62}–PEG_{3000}), reveals the channel diameter of the 6-HB to be 1.90 nm as measured theoretically. The increasing concentration of PEG and other ions in the conductive solution influences the greater conductance value brought about by bigger PEG molecules (PEG_{3000}).[58] Furthermore, majority of these DNA channels had a high conductance state between −60 and +40 mV, and the channel conductance drops dramatically when the applied potential is > +60 mV. Molec-

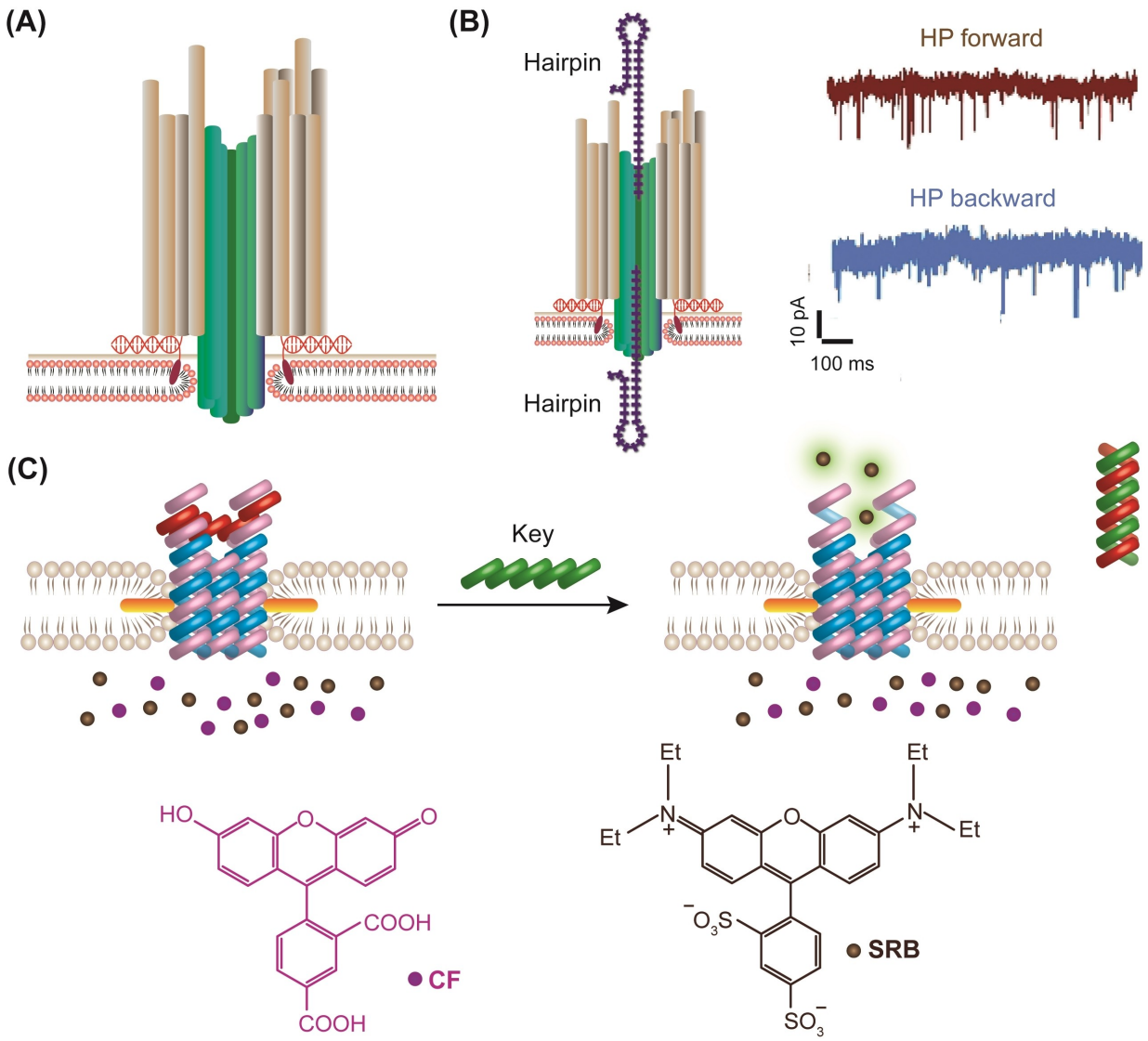

Figure 1. CaDNAnano based synthetic DNA transmembrane channel incorporated in an artificial lipid bilayer. (A) 1,2-diphytanoyl-*sn*-glycero-3-phosphocholine (DPhPC) bilayer insertion of the stem-and cap shaped DNA origami channel carrying 26 cholesterol molecules; (B) Electrical traces of the single DNA origami channel showing the successful translocation of the DNA hairpins (T5-HP-T50) both in the forward and reverse directions; and (C) DNA-triggered and charge selective release of the cargo molecule from the closed nanopore (NP–C) embedded in the small lipid vesicle system. The release of the cargo occurs on complementary binding of the key strand to the lock strand embedded in the closed nanopore. The fluorophores sulforhodamine B (SRB), carboxy-fluorescein and cholesterol molecules are marked in brown, magenta and golden yellow, respectively. (A and B) Reproduced (modified) with permission from the corresponding author ref. 10. Figures were redrawn completely; and (C) Reproduced (modified) with permission from the corresponding author ref. 60. Figure was redrawn completely.

ular dynamics (MD) simulations have recently been employed in an atomistic approach to confirm the molecular basis behind this voltage switching phenomena.[59]

Burns and colleagues created a DNA-like valve that attaches to a specific ligand on a DNA origami channel to enhance selective transport. The key oligos trigger the DNA nano-channel, allowing the transport of specific molecules.[60] The authors demonstrated open and closed confirmation experimentally by förster resonance energy transfer (FRET) and electrical recordings. To achieve selective transport and to match the thickness of the lipid membrane the authors reduced the height of the previous 6-HB from 42 to 9 nm. The nano channel (NP–C) is closed using a strand called 'lock-ssDNA', which is hybridized to the strands near the nanopore entrance. The addition of a key strand to the lock renders the channel to remain in the open confirmation (NP–O). Electrical recording shows that the nanopore in the closed confirmation (NP–C) produced clean ion-current channels with a conductance of 0.67 nS, alternatively, the nanopore in the NP–O produced a higher conductance of 1.61 nS. Transport assays show successful permeation of the positively charged sulforhodamine B (SRB) dye through the NP–O channel. However, the negatively charged 6-carboxyfluorescein shows 13-fold reduced transport through the NP–O channel revealing the charge selective nature of the nanopore (Figure 1C). Following this pioneering work, Mendoza and his group used the same 6-duplex DNA

channel to understand the permeation of positively charged SRB in the open and closed conformation of the channel. The patch clamp assays showed that the average channel conductance in the closed state was 0.3 nS and the open form produced a slightly higher conductance of 0.5 nS.[61] Similar studies were conducted by Wang *et al.* where they used a DNA origami rectangle to build a nano-shutter DNA channel which controls the transport of enzyme mediated oxidation reaction.[62]

In several nanopores[11,32,54,63] the helices follow a parallel arrangement, limiting the size of the DNA channel lumen. Dey and his colleagues were able to overcome this problem by using a horizontal routing procedure to create square-shaped nanopores.[64] They employed a lock and key mechanical approach to open and close the square DNA origami plate. A single duplex DNA with the dimensions of $70\times70\ nm^2$ was used for the fabrication of a square shaped DNA origami plate. For effective membrane piercing, the cap section of the origami plate was adorned with large number of hydrophobic anchors (N = 64). A flexible lid was attached to one side of the DNA plate while the other lid side features two ssDNA locks that can hybridize with the complementary strands to produce a complete duplex lock. They found out that the cholesterol labelled nanopore with the lid-on (LGC–O) produced 4-folds higher conductance (2.3 nS) with more electric current fluctuations than the nanopore with the lid-off (LGC–C, 0.64 nS), implying more ion permeation in the open nanopore system. However, the nanopore devoid of lid (LGC–N) generated two distinct channels with conductance of 2.51 and 5.92 nS, respectively. The lack of insertional activity in control experiments with a capless DNA square origami plate implies the significance of the cap portion in nanopore formation. Furthermore, the authors demonstrated that their nanopore, close and open in a step-like fashion when appropriate ssDNA key strands are added. The LGC–O nanopore was closed when the reverse key DNA strands were added, lowering the current to 17 pA at +10 mV. Alternatively, the channel was opened by introducing open key strands, which resulted in a current transition from 9 to 147 pA at a negative transmembrane potential of −10 mV. Transport assays with proteins in the LGC–O system shows that both trypsin and green fluorescent protein (GFP) produces bumping (type I) and translocation (type II) events whose translocation rate depends on the voltage applied. In parallel, fluorescence microscopy experiments also confirm the translocation property of these proteins. Thus, a more sophisticated DNA nanopore based cargo transport was brought by the authors whose nanopore design strategies might open new avenues for synthetic channel beyond nanopore sensing.

Most DNA origami channels are fabricated to generate channels with smaller conductance, Keyser and his team created a giant funnel-shaped DNA channel that punctures lipid bilayers giving the largest conductance of any known existing synthetic channel. Their 5 MDa DNA origami was constructed on a square lattice with an internal diameter of ~6 nm anchored with 19 cholesterol moieties. Despite the pressure in solvent-containing membranes, DNA constructs were able to form channels with a unitary large conductance in the 30–40 nS range (Figure 2A). At voltages greater than +50 mV, the channels switched to lower conductance state. Confocal imaging was also performed to illustrate the membrane penetrating potential of these DNA channels. The Cy3-labelled DNA cholesterol anchored channels appear as bright rings on the surface of giant unilamellar vesicles (GUV's) leaving the background colorless, whereas the cholesterol free channels appear free-floating in the solution. The atomistic calculations of the DNA channel through MD simulations, predicted that the majority (80%) of the ion-flow occurred through the central channel system.[32]

Earlier studies on DNA nanopores were concentrated on translocating nucleic acid materials, however, Diederich's *et al.* fabricated a DNA origami channel, which facilitated the transport of large folded proteins.[11] To attract larger proteins, the channel was constructed in a square lattice with a wider pore lumen measuring about ~7.5 nm^2 in diameter, 46 nm in length and 22.5 nm in width (Figure 2B). TEM measurements were used to verify the geometric assembly and the marriage between the cholesterol (N = 26) decorated DNA channels and small unilamellar vesicles (SUV's). Ionic-current measurements of these nanopores in painted bilayers produced channels with both higher and lower channel conductance of 2.37 and 1.18 nS, respectively. Switching between the high and low conductance states is noted at voltages > +80 mV. Protein sensing experiments revealed that trypsin and GFP, yielded non-translocating (bumping, type I) events, which occurred on both positive and negative transmembrane voltages, while the translocating (type II) events took place only on negative voltages. Due to the larger length of the GFP the average blockade of type II events was higher compared to trypsin molecules. Besides nanocapillaries, the authors used nano sized silicon-chips for size-specific transport properties of the DNA nanopores. The silicon chip uses the properties of cavity filled fluorescent probes, which allows passive diffusion of the molecules on insertion of DNA channels. Single-exponential fluorescent decay for enhanced GFP shows 5-fold higher influx through the DNA channel when the protein was tagged with the α-His antibody, on the other hand, the bulky rhodamine B dextran causes no significant variation in the fluorescence signal.

Recently, Thomsen *et al.* constructed the largest DNA origami channel, which accommodate proteins of size more than 150 kDa.[63] The channel was constructed from a double layered pseudo-symmetric hexagonal DNA lattice with a width and outer diameter of 9 and 22 nm, respectively. These structures contributed to elongated assembly (A and B), where the authors mix two individual components (A + B) of the structures in solution, giving rise to completely assembled one. To stick to the hydrophobic region of the POPC bilayers, the channel was designed to have three programmable flaps which are closed by the staple strands and opened by the addition of key strands through strand-displacement reaction. In addition to electron microcopy measurements, the authors used a Cy3–Cy5 pair-based FRET assay that opens the flaps quickly on addition of the key strands, thus, adhering to the tunnel like

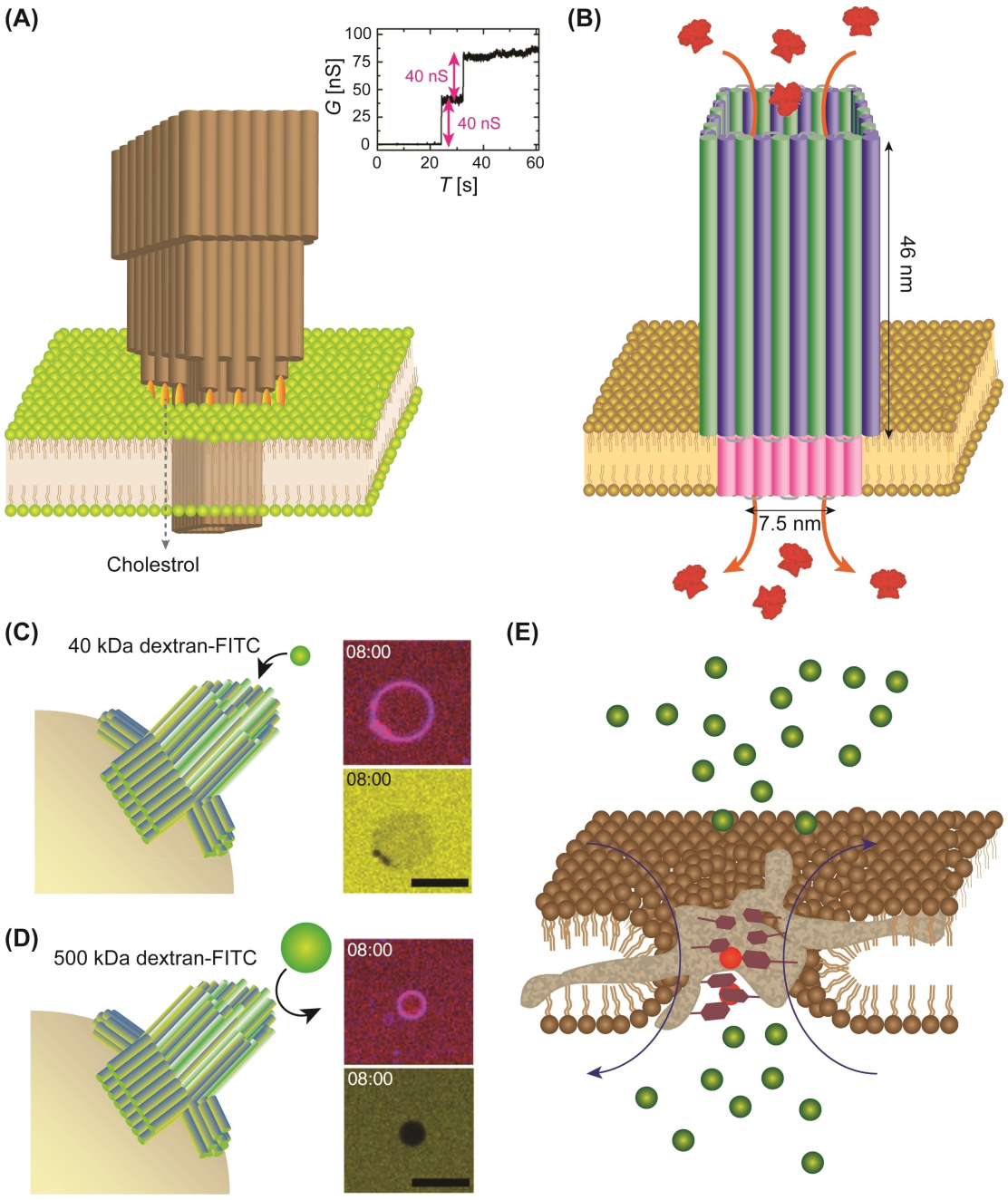

Figure 2. (A) Schematic of the tall 5-MDa funnel-shaped DNA origami using square-shaped DNA template. The DNA origami is inserted with the help of 19 cholesterol anchors (golden yellow). The corresponding step-wise insertions of 40 nS conductance in 1 M KCl buffer (Right figure); (B) Diagrammatic view of the square lattice designed rectangular nanopore composed of cap and cholesterol (N = 24) containing hydrophobic portion for membrane penetration. Trypsin (red balls) passes through the pore from *cis* to *trans* side; (C and D) Dye-influx assay showing the incorporation of the large pseudo symmetric hexagonal DNA nanopore with programmable flip-flops in giant unilamellar vesicles (GUV's) using sulforhodamine B (SRB) and 40-kDa dextran–fluorescein isothiocyanate (FITC). Time-dependent confocal images of SRB (red), Cy5-labeled DNA nanopores (blue) and FITC (yellow). Smaller cargo (40 kDa dextran-FITC) translocate through the nanopore (C, top right) whereas, larger molecules (500 kDa dextran-FITC) are excluded from the entry (D, bottom right); and (E) Transport of K^+ ions through the h-TELO G-quadruplex molecule adhered to the DPhPC bilayers by guanosine derivative (MG) though lipophilic chains (light brown). K^+ and Cl^- ions are shown in green and red, respectively. (A) Reproduced (modified) with permission from ref. 32. Copyright (2016) American Chemical Society, Creative Commons Attribution CC-BY license; (B) Reproduced (modified) with permission from ref. 11. Copyright (2019) Springer Nature Ltd., Creative Commons Attribution CC-BY license; (C and D) Reproduced (modified) with permission from ref. 63. Copyright (2019) Springer Nature Ltd., Creative Commons Attribution CC-BY license; and (E) Reproduced (modified) with permission from ref. 67. Copyright (2020) Springer Nature Ltd., Creative Commons Attribution CC-BY license.

structures into the POPC-based vesicle. Total internal reflection fluorescence microscopy measurements were carried out to confirm the docking and insertion of the ATTO 488 tagged DNA nanopores into the passivated SUV's. Dye-influx assay revealed the rapid uptake of SRB (0.5 kDa), into the Cy5-tagged nanopore system, whereas dextran-fluorescein isothiocyanate (FITC)

molecules of 40 or 1000-fold larger than SRB does not exhibit any changes in the fluorescence experiments. Likewise, the 40-kDa FITC dye was successfully translocated, albeit at a considerably slower rate, whereas the 500-kDa dye was large enough to exhibit any sign of translocation (Figure 2C and D). As a result, size selective influx was performed by inserting a molecular plug of PEG-20 kDa into the DNA pore via staple strand overhangs, contributing for the permeation of only SRB. Passivated SUV's loaded with ATTO 655 dye and 40-kDa dextran tetramethylrhodamine (dTMR-40k) further revealed the breadth of size-specific cargo translocation properties. Following DNA pore insertion, complete efflux of the cargo was achieved, but dTMR-40k remained entrapped when succinct-hemolysin pores were employed as a control. The loaded dTMR-40k was also released when the pore was unplugged by toehold-mediated strand displacement reaction.

However, a more advanced and functional DNA nanopore system has been constructed with the help of external trigger by Lanphere *et al.*[65] Their DNA nanopore system consists of two individual subunits A and B, made from two DNA strands which forms a central pore region of 0.8 nm wide. The DNA nanopore could self-assemble from the individual components of the ssDNA arms (A subunit) and the DNA loop (B subunit) either at the membrane interface or in the aqueous solution using the external trigger. The pre-assembled nanopores from two individual subunits (A + B) resulted in a single channel conductance of 0.70 nS. This conductance is similar to the nanopore ($AL^A + AL^B$) formed at the membrane interface by the addition of key strands ($K^A + K^B$, external trigger). Transport assays, with Ca^{2+} sensitive dye, Fura-2 shows higher influx (~ 90%), when the SUV's are mixed with assembled DNA origami system and the triggered DNA origami (75 nM). However, experiments with SRB reveals slower dye transport (~5%), even when higher concentration (400 nM) of assembled DNA origami subunits and the triggered DNA origami where used. This suggests the narrow lumen of the DNA origami nanopore permeates the small sizer of the Ca^{2+} dye more effectively than SRB. Control experiments showed no permeation of dye in the system, when SUV's are mixed with individual subunits of DNA origami system and the assembled DNA origami in the absence of key strands ($K^A + K^B$). This was further validated through MD simulation studies. Although triggered DNA nano objects does not exists in biology, these synthetic nanopores could be of great potential in benefitting the field of synthetic and chemical biology. The same research group constructed a similar subunit fashion like DNA origami nanopore which could sense larger biomolecules such as bovine serum albumin (BSA).[66] They fabricated a wider DNA origami whose subunits can be adjusted in size to provide a channel lumen from 43 nm^2 for a triangle to 400 nm^2 leading to a square form. This version is 260-fold larger than the typical α-hemolysin utilized in sensing experiments. For successful membrane puncturing, the nanopore also has a cap and a barrel adorned with cholesterol anchors. Single-channel electrical recordings showed large non-fluctuated channels of 4.5 and 8.9 nS were generated by square shaped DNA nanoconstructs (Sqr-10, 20), while triangular (Tri-10) shaped nanopores formed smaller channels of 2.10 nS. On treatment with anti-biotin-antibodies, the square shaped DNA nanopore labelled with biotin produced clean ion-current blockades. On the other hand, nanopores without the biotin tag does not initiate any disruption in the electric signal. Further, voltage-dependent recordings show that the translocation of BSA is brought through electrophoresis. Additionally, these nanopores were also used to sense antibodies generated from severe acute respiratory syndrome coronavirus 2 (SARS-CoV-2) using the Oxford MinION chip. Addition of SARS-CoV-2 antibodies to the SARS-CoV-2 spike protein labelled triangular (Tri-20) shaped DNA nanopores produced higher blockades with an amplitude and dwell time of ~61.7% and 1.7 ms, respectively. Thus, these DNA based molecular constructs which allow for precise attachment of any number of recognition tags, have a tremendous potential to advance nanopore technologies which could benefit the field of single-molecule protein sensing.

Debnath *et al.* showed the feasibility of constructing a chemically active DNA-based ionophore, that selectively transports K^+ ions when embedded in synthetic and biological membranes.[67] The ionophore was created by combining a human telomeric G-quadruplex (h-Telo) with non-covalently linked lipophilic guanosine (MG), allowing the G-quadruplex molecule to bind to the hydrophobic region of the lipid membrane (Figure 2E). On treatment with bilayers containing KCl, these ionophores produced channels causing an open conductance of 1.6 nS, but showed insignificant transport properties with NaCl, LiCl, RbCl, CsCl and NH_4Cl ions. Furthermore, the addition of thiazole orange and cytosine caused the ionophore to detach from the membrane, but the process was recovered by adding multiple volumes of h-telo/MG substrate. It was concluded that the interaction between the ionophores and the ions in the buffer contributes to selective K^+ transport. Selectivity measurements further revealed the preference of cations over other metal ions in the order $P_{K+} > P_{Na+} > P_{Rb+} > P_{Li+} > P_{Cs+}$. Additionally, atomistic view of these interactions was scaled by MD simulations along with FRET, isothermal calorimetry measurements and melting analysis. Similarly, the authors previously constructed an ion-channel by assembling G–C residues.[68]

2.1.2. Non-cholesterol based DNA origami channels

As cholesterol moieties are excellent membrane anchors, most research on DNA nanopores has focused exclusively on cholesterol-based membrane insertion. Alternative membrane insertion strategies, such as, porphyrin,[69] ethyl-phosphorothioates (ethyl-PPT),[70] tocopherol[54] and streptavidin-biotin[54] conjugated lipid network systems have recently been explored. These strategies contribute to its simple, reliable and stable nanopore insertion. For instance, Burns *et al.* designed a 6-HB DNA origami channel using hydrophobic ethyl-PPT as the DNA backbone. As a result, the barrel had a hydrophobic belt composed of 72 ethyl-PPT groups (6-HB×12), allowing the nanochannel to span the lipid bilayer (Figure 3A).[70] This nanobundle produce a stable ionic-current with no noise on

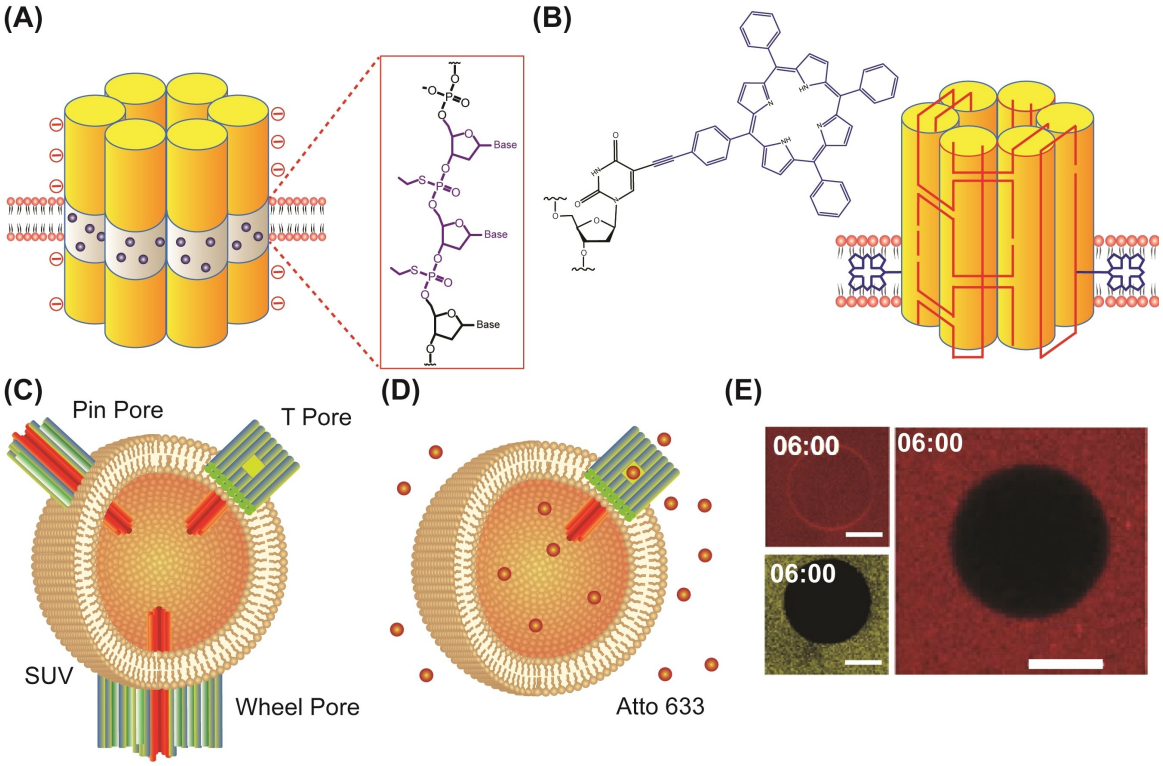

Figure 3. (A) Schematic showing the attachment of the 15 nm long and 2 nm inner diameter 6-helix bundle (HB) with ethyl-phosphorothioate (ethyl-PPT, magenta) groups. The insert shows the chemical structure of the DNA phosphate backbone modified with ethyl-PPT; (B) 6-HB showing the attachment of two ethyl tetraphenylporphyrin (ethyl-TPP) anchors (magenta) to deoxyuridine achieved through Sonogashira reaction; (C) Schematic representation showing the penetration of the pin-, wheel- and the T-pore channel on a small unilamellar vesicle (SUV); and (D and E) Dye-influx assays of the T-pore channel using surface immobilized GUV monitored through confocal laser microscopy. Increase in the fluorescence after the addition of ATTO 633 inside the GUV's containing the T-pore channels at t = 0 (top left); The larger fluorescein-dextran conjugate present in the surrounding medium is unable to enter the smaller GUV's (bottom); control experiments showing no dye influx without the T-pore addition (right). (A) Reproduced (modified) with permission from ref. 70. Copyright (2012) American Chemical Society; (B) Reproduced (modified) with permission from ref. 69. Copyright (2013). The authors. Published by Wiley-VCH Verlag GmbH and Co. KGaA, Weinheim; and (C–E) Reproduced (modified) with permission from ref. 54. Copyright (2016) Springer Nature Ltd., Creative Commons Attribution CC-BY license.

applying positive transmembrane potential (+100 mV). Moreover, these channels were extremely stable at voltages of up to 200 mV. Voltages >200 mV leads to the channel closure or detachment from the membrane. Additionally, when incubated with cervical cancer cells (HeLa) at a concentration of 60 μg/mL, these nanobundles diminished cell viability by 20% compared to the control 6-HB's, which lacks channel properties.[71] In addition, these DNA nanostructures have much lower cytotoxicity than several other pore-forming toxin proteins.[72,73]

Burns *et al.* renovated the 6-HB by relocating the hydrophobic section from the middle to the terminal region, permitting simple entry of the channel's hydrophobic region to the lipid membrane.[69] The authors used a Sonogashira reaction involving an acetylene-tetraphenylporphyrin (TPP) derivative and a deoxyuridine nucleoside (Figure 3B). Further, porphyrin contributes for increased hydrophobicity and cause them to shift their fluorescence emission when bound to lipid bilayers.[74] Due to their strong hydrophobic nature, they are used in fewer numbers for membrane penetration than conventional cholesterol molecules, which involves 26[10,63]/19/72-PPT molecules.[70,75] Under membranes formed by nanocapillaries, GUV's painted nanopores yielded an average conductance of 250 pS. However, ethyl-PPT modified 6-HB was marginally greater, ranging between 298 and 492 pS. The following considerations explains the difference in conductance between the two nanobundles with the same architecture, (i) The TPP moieties are present in the terminal section of the nanopore-membrane insertion, alternatively, the ethyl-PPT anchors are located at the central region of the 6-HB (Figure 3A and B); (ii) the flexible motion of DNA cause the nanopore slightly tilted rather than orienting perpendicularly in the membrane; and finally (iii) the bilayer system type also influence the variation in the conductance pattern. Most DNA origami channel's experimental conductance deviates from theoretical principles, which are largely determined by the pore width, length and molar conductivity of the solution.[76] These models continue to be ineffective at predicting the constant mobility of ions in nanomaterials with higher aspect ratios.[55,77] Furthermore, variations in the pore insertional angle and the lateral membrane pressure that determines the channel insertion resulted in a broad spectrum of channel conductance in DNA nanostructures.

Using the caDNAno program Krishnan *et al.* built a larger ~4 nm DNA nanochannel based on tocopherol anchors.[54]

Additionally, they also use the biotinylated lipid-streptavidin conjugation reaction for channel insertion as an alternative to cholesterol anchors, which causes DNA nanostructures to cluster. The T-DNA channel consists of a double-layered origami plate (46×51 nm^2) connected to 12 helices, generating a 27 nm long stem region that penetrates to the membrane. For ease penetration of the structures to the POPC vesicles, the bottom of the origami plate was fixed with 57-tocopherol moieties. In parallel, by modifying the previous version of DNA nanostructures, the authors created pin pores with 6-HB and wheel DNA nanochannel with an inner diameter of ~2.6 nm (Figure 3C). Droplet-interface bilayer approach using DPhPC vesicles displayed higher insertion frequency for T-channel with a larger conductance of 3.1 nS. While the pin and the wheel pore showed a smaller channel conductance of 1.6 and 1.5 nS, respectively. Also, the big T-pores have the unique ability to insert from the outside-in and inside-out configuration allowing successful dsDNA translocation with a reduction in residence time from 170 to 149 μs in response to the applied electric potential from 75 to 125 mV. Dye influx measurements using GUV's of about 10 μm were also performed to access the transport behavior of the designed DNA origami channels, which disclosed that larger T-pore and wheel pore were able to induce the influx of membrane impermeable dye, ATTO 633, whereas the pin pore shows little or no flux, in consistent with the pore size (Figure 3D and E).

2.2. DNA nanopores formed from nanocapillaries

Laser-assisted nanocapillary pulling can be used to create well-controlled nanoscale channels, allowing for the easy fabrication as an alternative to existing silicon based solid-state nanopore devices. Nanopores formed from nanocapillaries have gained increasing popularity, especially for DNA origami devices due to its cost-effective process. Recently, Raveendran *et al.* demonstrated the potential of glass nanocapillaries in detecting structural differences between two different DNA origami structures (frame from tile) (Figure 4A) depending on the differences in the current amplitude and dwell time.[78] The designed DNA origami constructs differ only in their shape but not in the mass or charge. The nanocapillaries trapped both the DNA tile (40×40 nm^2) and frame origami (80×80 nm^2) constructs through the top portion of the nanopore by applying a negative bias voltage (−350 mV). The tile structures produced a higher ionic current of ~65 pA than the frame structures of ~59 pA, contributing to the geometrical difference. Additionally, they concluded that the tile structures were able to translocate at a faster rate than the frame structures.

To further improvise the frame origami design, the authors made a cavity at the center of the square shaped origami structures for detecting human inflammatory biomarker, the C-reactive protein (CRP). Three DNA tiles were assembled to design concentric square shaped origami structures as ConA, ConB and ConC, where ConB and ConC differ in the design by having a central cavity of 30×12 nm^2 and 65×25 nm^2, respectively. Translocation experiments using nanocapillaries suggest that ConA with no cavity translocates rapidly through the nanopore with a short dwell time of 0.15 ± 0.01 ms, whereas ConC with a larger central cavity translocates slowly with a long dwell time of 0.31 ± 0.14 ms. For detecting CRP, the square shaped origami (cavity dimension, 35×35 nm^2) was designed to have additional staple strands complementary to the CRP-DNA domain. Upon nanopore measurements, the square DNA nanostructures with no CRP occupancy produced a single peak of 65 pA at a translocation rate of 0.29 ± 0.1 ms, whereas two characteristic ion-current peaks of 62 and 90 pA with a dwell time of 0.33 and 0.15 ms indicates the detection of the CRP near the cavity of the DNA origami (Figure 4B and C). Thus, the authors were able to demonstrate the difference in the analyte detection between the origami designs with and without cavity through changes in the peak shape, current-amplitude and dwell time.[46]

Hernández-Ainsa *et al.* developed a strategy of forming hybrid nanopores in a reversible fashion by incorporating DNA origami nanoplates onto the nanocapillaries. The designed DNA nanoplates enabled them to tailor pore size of any desired specificity, thus avoiding the need of TEM drilling for nanopore formation. They incorporated two rectangular DNA origami nanoplates with the same outer dimensions of 60×54 nm but differed only in the nanopore diameter (14 and 5 nm) into glass nanocapillaries. A drop in the ionic-current with an increase in the current noise on the application of +300 mV indicates the trapping of the DNA origami into the nanocapillary system. The origami was untangled several times by applying a high negative bias voltage of −1000 mV, which leads the current level to return to the initial state (Figure 4D and E). The electrical recordings were also combined with optics in such away they labeled the DNA origami structures with Cy3 fluorophores.

Additionally, translocation of biomolecules can be effectively controlled through tuning of the pore size. In an attempt to do so, the authors showed that linear ds λ-DNA of 48.5 kbp undergoes several folding until attaining translocation through the hybrid nanopore of 14 nm in size, however, the process of folding is limited in the case of 5 nm hybrid nanopore system revealing the smaller diameter of the origami as the limiting factor (Figure 4F). Moreover, they impart chemical functionality to these hybrid nanopores by attaching ssDNA overhangs to the 14 nm nanopore system. These sequence forms the binding sites for the ssDNA as they form complementary sites, which significantly increases the residence time of the translocated molecule. A longer residence time can be achieved by increasing the length and sequence attached to the nanopore system.[79] By further exploiting the nanocapillary potential, Youn *et al.* used the same sequencing strategy with the nanocapillary free from DNA origami structures for DNA translocation under controlled temperature system.[80]

In an extension of the previous study,[79] the same group showed that hybrid DNA origami nanopores change their confirmation leading to control over biomolecular translocations in response to the applied electric potential. Ionic-current drop was recorded when a flat two layered rectangular DNA origami nanoplate of outer dimensions 54×60 nm^2 with a

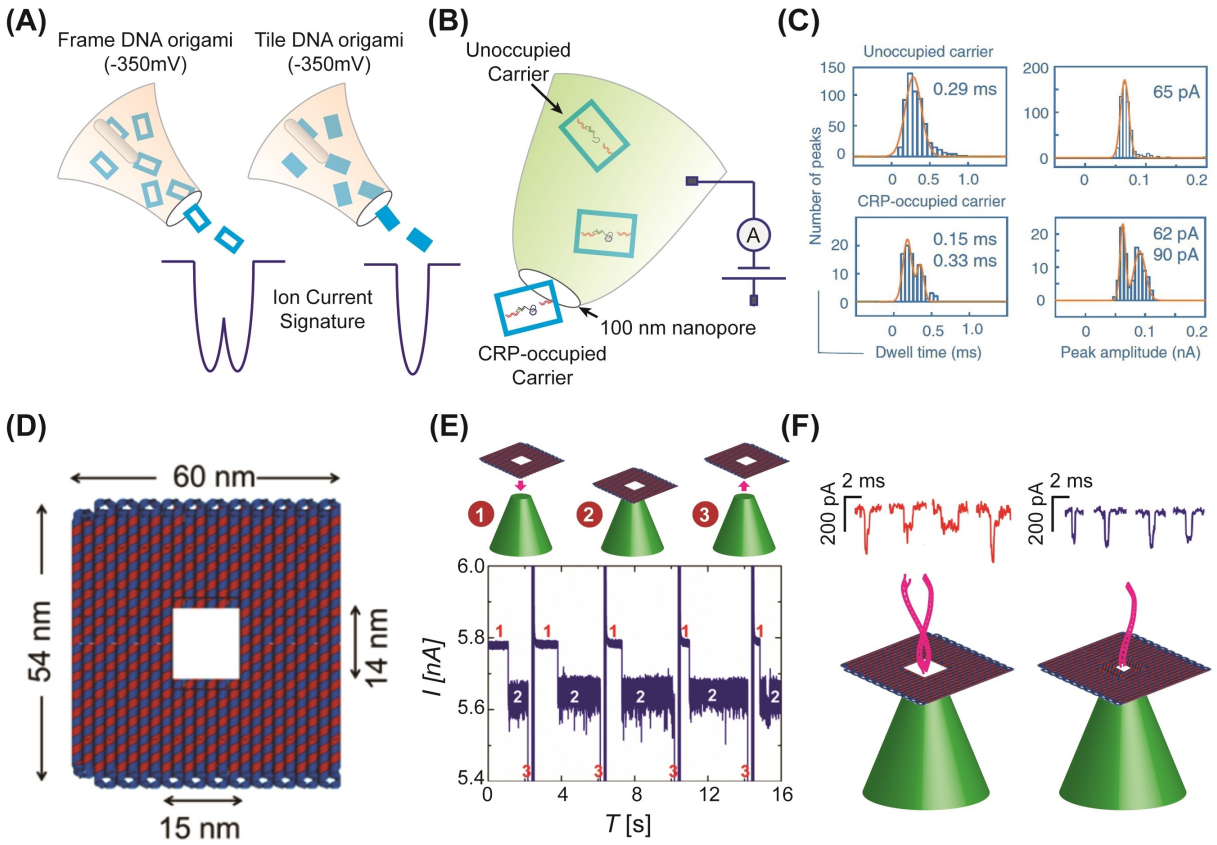

Figure 4. (A) Diagrammatic representation showing the translocation of frame shift (left, blue open) and tile-based (right, blue closed) DNA origami nanostructures through bilayers formed using nanocapillaries; (B) Graphical view of the square shaped DNA origami nanostructure as translocation carriers in biosensing through nanocapllaries; (C) Peak amplitude and dwell time histograms of DNA nanostructure carriers (9 nM) and carriers incubated with C-reactive protein (CRP, 9 nM), both measured at a final carrier concentration of 500 pM; (D) Schematic representation of the square shaped DNA origami nanostructure with a pore size of 15×14 nm and dimensions of 60×54 nm, respectively; (E) (Top) Pictorial representation showing the reversible and repeated trapping and ejection of the flat shaped DNA origami nanostructure onto the glass nanocapillary in 1 M KCl buffered with pH 8.2. (Bottom) The corresponding electrical trace of the flat-shaped DNA origami nanostructure. (1) Ionic-current showing no trapping of the DNA origami structure at 300 mV; (2) Ionic-current showing the successful trapping of the DNA origami structure onto the glass nanocapillary at 300 mV; and (3) Ionic-current showing the ejection of the DNA origami plate from the nanocapillary on applying a high negative voltage of −1000 mV; and (F) Typical λ-DNA translocation events through the hybrid nanopore of diameter 14 (red, left) and 5 nm (violet, right), respectively. The size of the nanopore influences the folding behavior of the λ-DNA as it translocates through it. (A) Reproduced (modified) with permission from ref. 78. Copyright (2018). Published by Wiley-VCH Verlag GmbH and Co. KGaA, Weinheim; (B and C) Reproduced (modified) with permission from ref. 46. Copyright (2020) Springer Nature Ltd., Creative Commons Attribution CC-BY license; and (D–F) Reproduced (modified) with permission from ref. 79. Copyright (2013) American Chemical Society.

nanopore region of 14×15 nm^2 was trapped on the nanocapillary through applied electric potential between 300 and 800 mV. The central nanopore region was left alone with a long dsDNA tail measuring about 450 nm. The folding of the caDNAno designed DNA origami plates were confirmed through AFM. Current histograms of the current drops showed single population of cells at both lower (300 mV) and higher voltages (800 mV), but significantly higher current drop at higher voltages (800 mV). Interestingly, two populations of ionic-current values were recorded for intermediate voltages running from 400 to 700 mV (Figure 5A and B). However, the nanoplates translocated successfully through the capillaries at voltages >800 mV (Figure 5C). The authors concluded that the two state behavior was due to the deformation of the DNA origami above a certain threshold potential, which can also lead to successful translocation of the origami nanoplate into the nanocapillary. Additionally, translocation experiments with ds λ-DNA showed that the hybrid nanopore system reduces the translocation efficiency by 1-fold.[81]

The preceding study was further exclusively elaborated by Aksimentiev and his team where they combined MD simulations with electrical recordings and FRET measurements. They looked at how the number of layers in the origami plate, nucleobase composition, lattice type and Mg^{2+} ion concentration affected ion conductance. They concluded that: (i) the conductance of the two layered DNA origami plate is directly proportional to the applied voltage due to the lower volume occupancy of the DNA than the four and six layers, which showed no significant variation in the conductance. Such higher DNA layers in the origami plate make the design more compact, thus, making less favorable for the movement of ions; (ii) the square lattice-designed origami plates showed two-fold increased conductivity than the structures created using the honey comb lattice profiles, which is also well corroborated by MD simulation studies; (iii) the ionic-conductance strongly

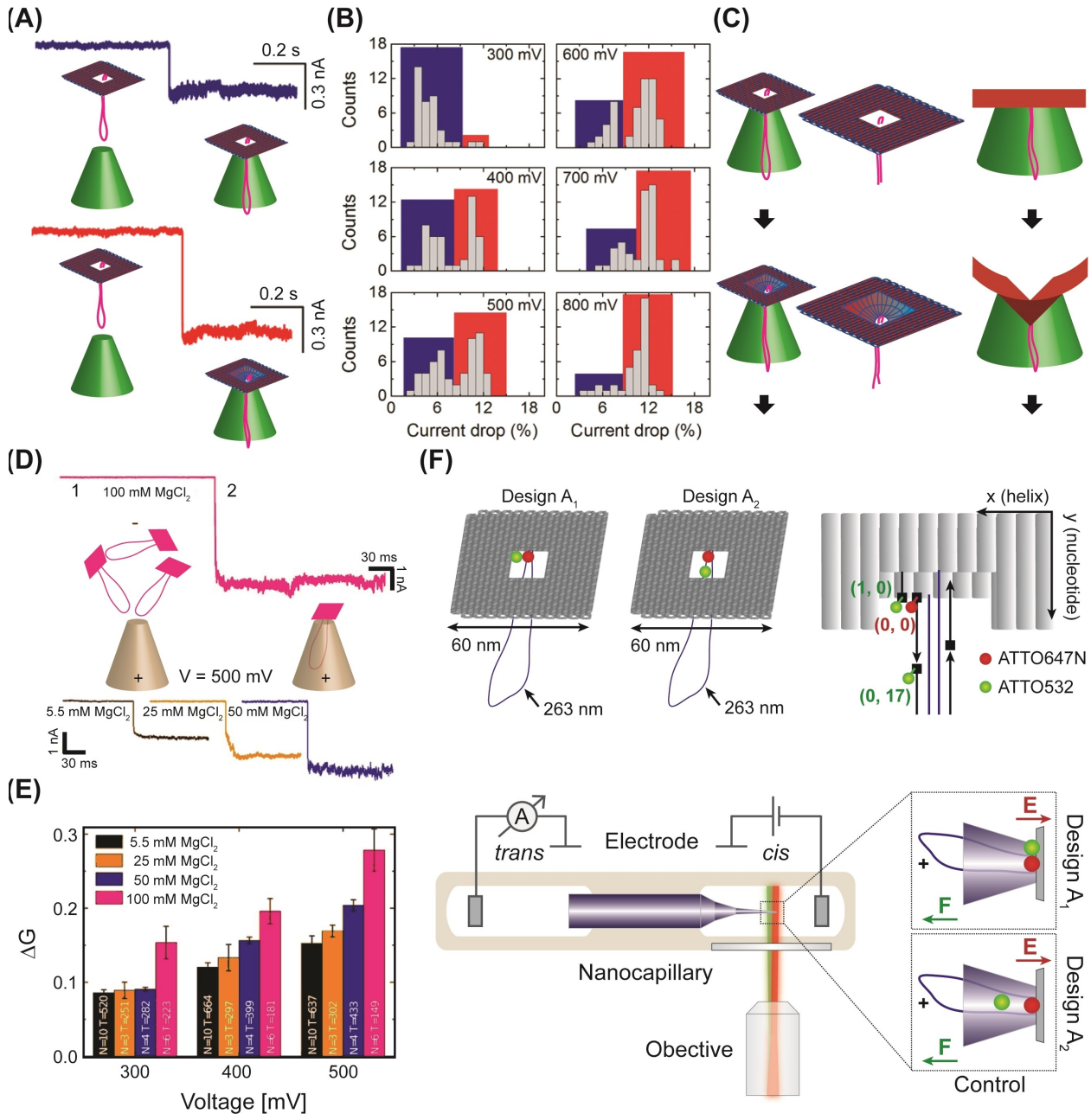

Figure 5. (A) Typical ion-current trace and schematic representation showing the trapping of the flat-shaped DNA origami nanostructure of dimensions 60×54 nm onto the glass nanocapillary. The trapping results in two types of ion-current drop namely lower (violet) and higher (red) on applying a potential of 400 mV. The DNA origami nanostructure has a leash of 1.34 kb (450 nm) attached onto it for its easy trapping onto the glass nanocapillary; (B) All-points histogram showing two different populations (lower- violet and higher- red) of ion-current drop events on trapping the DNA origami nanostructure onto a single nanocapillary at voltages ranging from 300 to 800 mV. The area of the drop indicates the amount of ion-current drop executed by both the populations. Single population of ion-current drops were observed at lower (violet, 300 mV) and higher (red, 800 mV) voltages. Both lower (violet) and higher (red) ion-current drops were observed on trapping of the DNA origami plate onto the nanocapillary at intermediate voltages (400–700 mV); (C) Schematic showing the two-state proposed conformations of the trapping of the DNA origami nanoplate onto the glass nanocapillary depending on the voltages applied. First conformation (top): Trapping of the DNA origami nanoplate with its sheet section flat but fluctuating near the tip of the nanocapillary. Second conformation (bottom): Buckling and partial introduction of the trapped DNA origami plate onto the glass nanocapillary; (D) Schematic representation showing both the trapping of the square-shaped DNA origami onto quartz-nanocapillary and its corresponding ionic-current traces measured at 500 mV in 1 M KCl, buffered with 100 mM $MgCl_2$ and 0.5 X TBE (Tris/Borate/EDTA (ethylene diamine tetraacetic acid), pH 8.3. Electrical trace (part 1: Ion-current flowing through the bare quartz-nanocapillary; and Electrical trace (part 2): Ion-current drop leading to the trapping of the DNA origami nanoplate on the nanocapillary; (E) Relative change in the ion-conductance in respect to increasing $MgCl_2$ concentrations and applied voltages. Higher current drops were observed with increasing voltages and $MgCl_2$ concentrations; and (F) Schematic design of the DNA origami plates for voltage-responsive fluorescent based sensing. Both the design (A_1 and A_2) has a pair of FRET dye labelled with ATTO 532 (green, donor) closer to the plate edge and ATTO 647 N (red, acceptor) closer to the central region of the nanoplate. The FRET dye pair is aligned perpendicular (design A_1) and parallel (design A_2) to the electric field. Live recordings were performed with the help of fluorescence microscope attached to the bilayer system. (A–C) Reproduced (modified) with permission from ref. 81. Copyright (2014) American Chemical Society; (D and E) Reproduced (modified) with permission from ref. 82. Copyright (2015) American Chemical Society; and (F) Reproduced (modified) with permission from ref. 83. Copyright (2018) American Chemical Society, Creative Commons Attribution CC-BY license.

depends on the type of nucleotide content in the DNA origami plate. The authors claimed that the AT plate tends to exhibit more leakiness while the CG plates makes the structure rigid and compact. Alternatively, the CG-rich origami plates tend to occupy high sources of Mg^{2+} molecules, thus, reducing the electrostatic repulsion between the helical bases in the origami design; (iv) The magnitude of the current drop of the hybrid origami-nanocapillary structure increases as the concentration of the Mg^{2+} is increased. The ΔG ($\Delta G = 1 - G_{hybrid}/G_0$, where G_{hybrid}/G_0 is the ratio between the conductance of the nanocapillary alone (G_0) and the conductance of the hybrid origami-nanocapillary (G_{hybrid})) of the hybrid structures increases exponentially with the increase in Mg^{2+} concentration and applied voltages (Figure 5D and E); and (v) direct influence of the applied potential on the DNA origami. This is documented, when placed on a SiO_2 material, the origami plates buckle and permeate through the nanopore because of the competition between the high applied voltage and the electro-osmotic flow.[82] Overall their study shows that the conductance properties and DNA nanopore leakiness can be efficiently regulated by rigorous DNA design principles, that can be applicable to several nanopore based sensing applications.

A step further, Hemmig *et al.* showed how one can tune the DNA origami structures in response to optical-voltage thus, making DNA origami as voltage-based optical sensor.[83] They constructed a nanocapillary based hybrid nanopore system that was able to convert the deformation of the DNA origami pore element, and so the applied voltage, into fluorescent optics. They were able to induce a fluorescent signal by attaching a FRET dye pair, ATTO 532 (donor, green) and ATTO 647 N (acceptor, red) on the pore forming section of the double layered DNA origami plate (170 bp $\times$24 helices), which was previously accompanied by a double stranded leash running on the central section of the nanoplate channel.[81] The fluorescent signal is greatly dependent on the distance between the attached dye pairs, which is directly influenced by the changes in the DNA origami plate as governed by the applied potential of the nanopore capillaries. Two different strategies were used to position the two dyes on the origami plate. In the first design, parallel alignment was adopted where ATTO 532 is placed at the edge of the plate with ATTO 647 N attached on the DNA leash (Figure 5F). Alternatively, these dyes were arranged in a perpendicular fashion in line with the electric field. The dye-tagged DNA origami plates were then attached to the glass nanocapillaries through applied potential ranging from 100 to 400 mV and their excitation phenomenon was confirmed from the fluorescence microscopy attached to the nanopore system. Both MD simulations and electrical measurements recorded a change in the dye excitation in response to the voltage applied, for the dye aligned in perpendicular fashion, while the parallel alignment did not show any significant change showing the sensitivity of the optical measurement. Recently, DNA based microcapsule produced through pickering emulsion stabilized with DNA nanoplate were designed to perform ion-channel function.[84] A hexagonal DNA origami plate coated with cholesterol molecules were used for the channel formation. These DNA origami plates self-assemble at the oil-water interface without the requirement of supporting membranes and thus, permeating ions between droplets in contact. This suggests the possibilities for engineering synthetic cells or molecular robots using DNA-based molecular constructs.

2.3. DNA nanopores docked into solid-state membranes (hybrid type nanopores)

Hall and Dekker were the first to introduce the concept of hybrid nanopore system.[28] The process involves the use of two nanopore systems such as protein/DNA docked onto a solid-state substratum, namely, the SiN. A double-stranded DNA is tied to α-hemolysin and pulled to the SiN membrane measuring with an applied transmembrane potential (mV). The mechanism of insertion involves three steps namely, phase 1: dsDNA translocations; phase II: pre-insertion of the protein channel; and phase III: stable insertion leading to stable channel conductance (Figure 6A and B). The hybrid nanochannel conductance was similar to the channel conductance of 1.0 nS, exhibited by α-hemolysin. A step forward without the involvement of double-stranded DNA tail, Cressoit *et al.* showed that voltage is sufficient to squeeze the portal protein G20c into the solid-state membrane. Such hybrid devices were able to translocate a wide range of analytes including proteins and DNA molecules (Figure 6C).[29]

However, hybrid nanopore systems involving the capture of engineered DNA origami onto SiN membranes were first introduced by Bell and Weil.[85,86] The method is similar to the one shown above which involves the entanglement of α-hemolysin into SiN membrane through electric potential. Bell *et al.* used four skirt funnel shaped origami with an overall length, outer and inner diameter of 51, 38.9, and 7.5 nm, respectively (Figure 6D).[85] A dsDNA of 2.34 kbp long is attached to the tip of the origami funnel, which aids in trapping the origami in the correct orientation onto the SiN membranes with diameters measuring between 13 and 18 nm. On applying a negative transmembrane potential, a single DNA origami structure gets trapped into the SiN device resulting in lower conductance than the conductance of the bare solid-state nanopore. Unlike protein channels, hybrid nanopores involving DNA constructs can be easily expelled and reinserted back into the SiN bilayer system by reversing the electric potential. Such expelling and reinsertion process can be conducted several times without clogging the bare solid-state nanopore, thus, making the docking process highly controllable and reversible. Translocation experiments with λ-DNA (48.5 kbp) showed that the λ-DNA undergoes structural folding in the bare SiN nanopore, on the other hand, the smaller inner diameter of the hybrid nanopore restricts the folding of λ-DNA (Figure 6E and F).

The flexibility and durability of solid-state membranes enable them to accommodate both simpler flat shaped and complex funnel-shaped DNA origami constructs. Contrary to the complex four-layer funnel-shaped DNA origami,[85] Wei and his group constructed a simpler flat shaped origami constructs

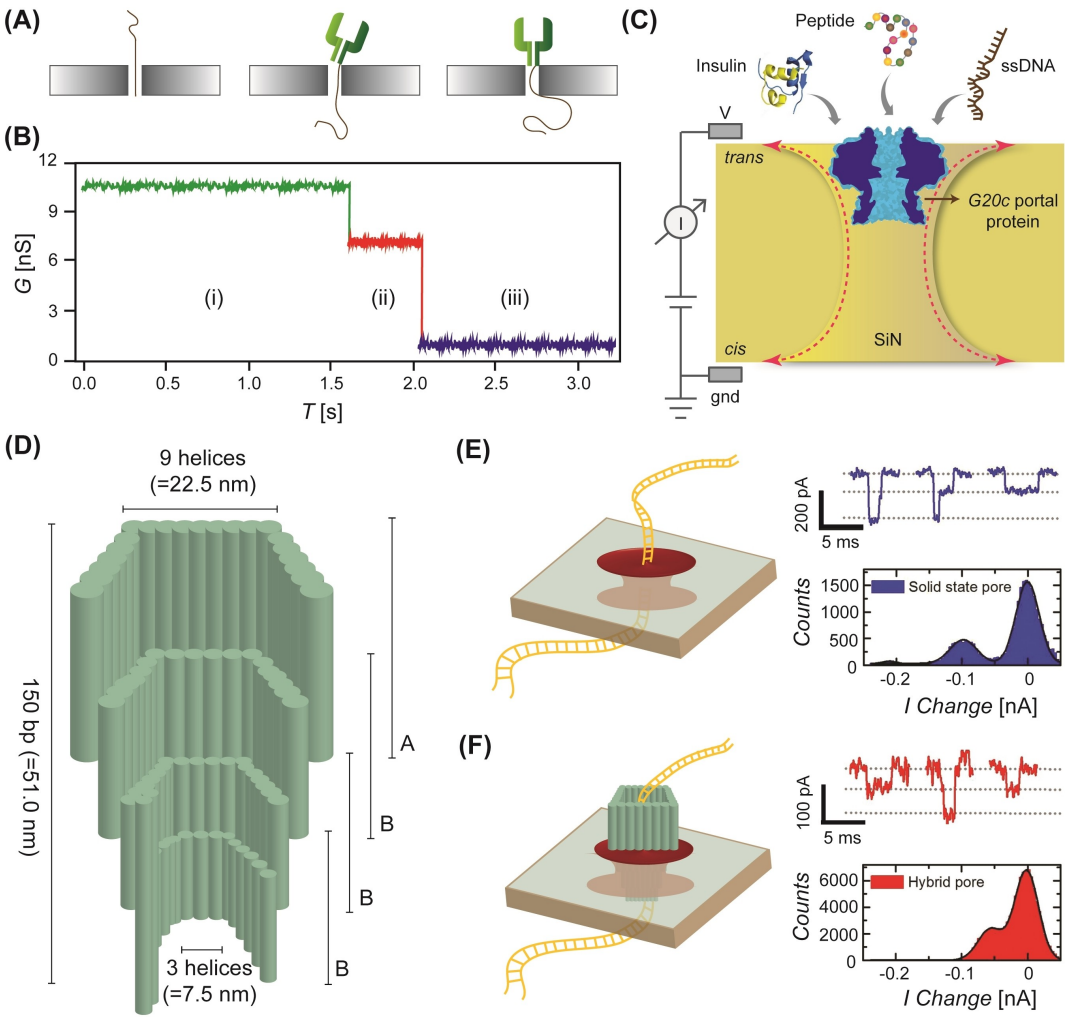

Figure 6. (A) Cartoon showing the insertional behavior of the mushroom-shaped α-hemolysin channel tagged with ds-DNA onto the silicon nitride (SiN) nanopore substratum. The corresponding electrical pattern observed during the insertional process is shown in (B). (B-i) Transient electrical output recorded due to the translocation of unconjugated ds-DNA onto the SiN nanopore substratum; (B-ii) These events were followed by a brief plateau of lower conductance which is concluded as the pre-insertional step; and (B-iii) the final lower conductance state of 1.0 ± 0.5 nS corresponds to the docking of the α-hemolysin channel onto the SiN nanopore system; (C) Schematic showing the insertion of the highly thermostable viral G20c portal protein onto the SiN nanopore system. The hybrid nanopore were able to successfully translocate biomolecules such as ssDNA, proteins and peptides; (D) Illustration of the funnel shaped DNA origami constructed using caDNANO on a square lattice. Dimensions of the funnel shaped nanochannel: 150 bp long (~51 nm long), 9 dsDNA helices wide (~22.5 nm) at the base and 3 dsDNA helices wide (~7.5 nm) at the tip. For the easy insertion of the origami into the SiN nanopore, the DNA origami has a long ds-DNA leash of 2.3 kbp attached on to it (not shown in the figure); (E) Typical schematic representation and the electrical traces showing the successful translocation of λ-DNA through the bare SiN (violet); and (F) hybrid nanopore system (red). The corresponding current-amplitude histogram showing the translocation of 43 events (violet) and 187 events (red) through the (E) bare SiN and the (F) hybrid nanopore. (A and B) Reproduced (modified) with permission from the corresponding author. ref. 28. Figures were redrawn completely. (C) Reproduced (modified) with permission from ref. 29. Copyright (2018) Springer Nature Ltd., Creative Commons Attribution CC-BY license; and (D–F) Reproduced (modified) with permission from ref. 85. Copyright (2012) American Chemical Society.

with and without apertures using the honey comb lattice (Figure 7A).[86] Such constructs act as gate keepers for solid-state nanopores. From single-molecule electrical measurements they found that the relative conductance of the nanoplate decreased as the pore size was reduced suggesting that the nanoplate was trapped inside the solid-state device in a flat orientation. In a similar fashion, they found that the nanoplates lacking a central aperture also caused a drop in the conductance of about 17%. Apart from dsDNA, nanoplates have been used as a sensing tool to detect molecules of high molecular weight, such as streptavidin, IgG and dsDNA (6 kbp) (Figure 7B). Streptavidin and dsDNA were able to translocate through the hybrid nanopore whereas, larger molecules >150 kDa (IgG) antibody were unable to translocate due to the smaller size of the nanoplate than the translocating biomolecule (IgG). Through bait-prey mechanism the authors were able to show that the DNA origami nanopores can be chemically challenged as highlighted by the sequence-specific detection of DNA bait enclosed in the aperture and the incoming prey sequence. The authors claim that the dwell time of the reaction strongly depends on the length of the prey sequence which forms base pairs with the DNA bait motifs used in the nanoplate aperture.

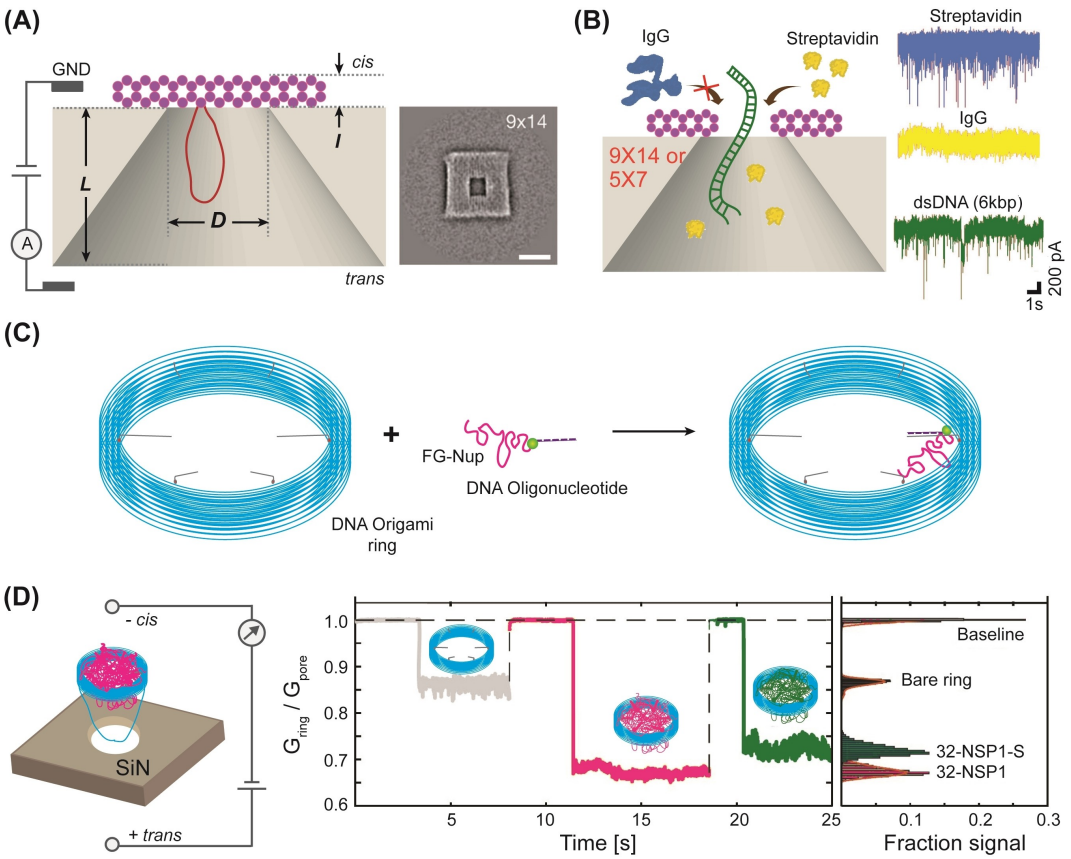

Figure 7. (A) (Top left panel) Schematic of the hybrid nanopore set up showing the DNA origami nanoplate (magenta) and the free-standing SiN nanopore (grey) system. The DNA nanoplate is left with 1.3 kb long dsDNA loop that passes through the central aperture for easy insertion into the SiN nanopore set up (L = 50 nm and D = 18–25 nm). (Top right panel) Negatively stained transmission electron micrograph of the DNA nanoplate with aperture size of 9 × 14 nm. Scale bar: 20 nm; (B) Size-selective biomolecular sensing using custom-made DNA origami nanoplates trapped on to the SiN nanopore system. Ion-current trace showing the translocation of streptavidin, IgG antibody and dsDNA (6 kbp long) onto the hybrid nanopore set up, whose DNA nanoplate aperture dimensions are 9 × 14 nm and 5 × 7 nm, respectively. Streptavidin and dsDNA were able to translocate through the DNA origami nanoplate but, IgG is retained due to the smaller aperture size; (C) Schematic showing the attachment of the intrinsically disordered proteins (FG-Nups) to the DNA origami ring constructed using 18 helices with an inner diameter of 34 nm. The DNA origami ring and one NSP1 protein is covalently linked with NSP1 protein; and (D) (Left panel) Hybrid nanopore set up showing the docking of the DNA origami ring onto a solid-state nanopore system. (Right panel) Single-channel electrical trace showing the change in relative conductance (G_{ring}/G_{pore}) achieved during the docking of the ring without protein (gray), 32-NSP1 (magenta) and 32-NSP1-S (green) onto a solid-state nanopore. (A and B) Reproduced (modified) with permission from ref. 86. Copyright (2012). Published by Wiley-VCH Verlag GmbH and Co. KGaA, Weinheim; and (C and D) Reproduced (modified) with permission from ref. 44. Copyright (2018) Springer Nature Ltd., Creative Commons Attribution CC-BY license.

Plesa *et al.* conducted a more detailed investigation on the ion-current leakage in a pore-less DNA origami nanoplate on docking into a solid-state nanopore.[87] It was observed that square lattice exhibits a higher leakage current compared to honey comb model. The observed relative conductance was slightly lower for a single layer square lattice model compared to two and three layers. The authors claim, that this is due (i) to the different arrangement of staple strands within the different structures; and (ii) the deformations of the DNA origami structure due to missing staple strands. The asymmetric I–V curve was due to the mechanical bulking of the DNA origami as the voltage is increased. This increase in the voltage leads to structural damage thus, making the structure to pass through the solid-state nanopore. They were able to show that the nanopore conductance was not influenced by the tail on the DNA origami nanoplate. This paper also investigated the effect of voltage ramping after hybrid nanopore formation. Higher voltages cause the nanoplate to undergo structural deformation and can be effectively translocated through the bare SiN having smaller pore diameter than larger ones. They also showed that the high Mg^{2+} concentrations are neither required for nanoplate stability nor it influences the docking of the nanoplate into the SiN nanopores.

Besides SiN, the graphene plates were also used to generate hybrid nanopores utilizing DNA origami objects. Farimani *et al.* employed a graphene sheet with a pore size of 2.1 nm to incorporate DNA origami. To better comprehend the ion-conductance and ssDNA translocation investigations, MD simulations were used against four different nanopore systems such as graphene layer, single layered DNA origami, single-layer DNA origami hybrid and double-layered DNA origami hybrids. Only at negative transmembrane potential, DNA origami aligns on top of the graphene sheet, where the alignment of the hybrid nanopore appreciably impacted. However, the authors arrested

this DNA origami motion by sandwiching the origami between the two layers of the graphene sheet. Translocation experiments with ssDNA (polydA, polydT, polydC, polydG) suggest that the translocation rate was in the order of bare graphene > single-layered DNA origami hybrid > double-layered DNA origami hybrid. This indicates that the translocating molecules spend a longer time in the double layered compared to the single-layered origami hybrid. The bait-prey mechanism was followed to understand the interaction of the translocating ssDNA with the nanopore system. The authors found the hydrogen bond interaction between ssDNA and the DNA nanopore contributes for the difference in the translocation time.[45]

Recently, Ketterer *et al.* constructed a synthetic DNA origami ring mimicking the function of the natural gate keeper, nuclear pore complex for the nuclear transport in eukaryotic cells.[44] The DNA ring consists of 18 helices and is attached with intrinsically disordered proteins known as FG-Nup (Figure 7C). The correct folding of the assembled DNA origami ring structures with FG-Nup was validated from TEM and cryo-TEM images. According to the fluorescence experiment, the intensity of the DNA ring grows as the number of attachment sites increases. Electrical measurements revealed that the DNA ring-protein complex can be docked into the SiN nanopore by applying an electric potential of +100 mV. The ion conductance blockade was high for the 32-FG-Nup (35±5%, 32-NSP1) in comparison to the 8-FG-Nup (20±4% for 8-NSP1) (Figure 7D). A mutant FG-Nup complex (NSP-1S) was also created by replacing the hydrophobic amino acids with serine. The weaker hydrophobic interaction of the DNA-protein complex causes a much-reduced ion-current blockade for both the mutant forms (8-NSP1-S and 32-NSP1-S) than the wild type. The experimental data are well aligned with the MD simulations performed for the ring nanopore system. Thus, these findings clearly demonstrate the ease with which DNA can be tuned to produce giant nanostructured materials that mimic biologically active counterparts, all of which could lead to the discovery of new therapeutic drugs.

2.4. RNA origami nanopores

Li *et al.* for the first-time used RNA as a potential tool for peptide sensing.[88] Two different strategies were adopted for the nanotube design. In the first approach, the RNA nanotube was constructed using 6 RNA strands with an inner and outer diameter of 1.7 and 6.3 nm (Figure 8A), respectively. Alternatively, they constructed another RNA tube whose 6 RNA strands were made to hybridize with other RNA strands having the same internal diameter. RNA tubes (cholesterol$^+$) mixed with unilamellar vesicles exhibited discrete ion-current jumps producing a channel conductance in the range of 3–4 nS in 1 M KCl (Figure 8B). Like DNA channels, the frequency of ion-current jumps was facilitated by the increase in the number of cholesterol anchors. These RNA nanotubes bind and internalize the cell membrane of human prostate cancer cell lines (LNCap). Strong electrostatic force of attraction between the RNA and TAT peptide (CYGRKKRRQRRR) complex resulted in significant ion-current blockage, with little or no blockage for both positive and neutrally charged peptide molecules. Thus, RNA nanochannels can be used as an alternative platform in sensing applications in replacement of DNA origami nanopores.

3. DNA nanopores stability in biological media

Despite the ease in the construction of DNA origami objects, the bio-applications of the constructed DNA architects are constantly under debate due to the following two main reasons: (1) poor survivability in media containing lower Mg^{2+}

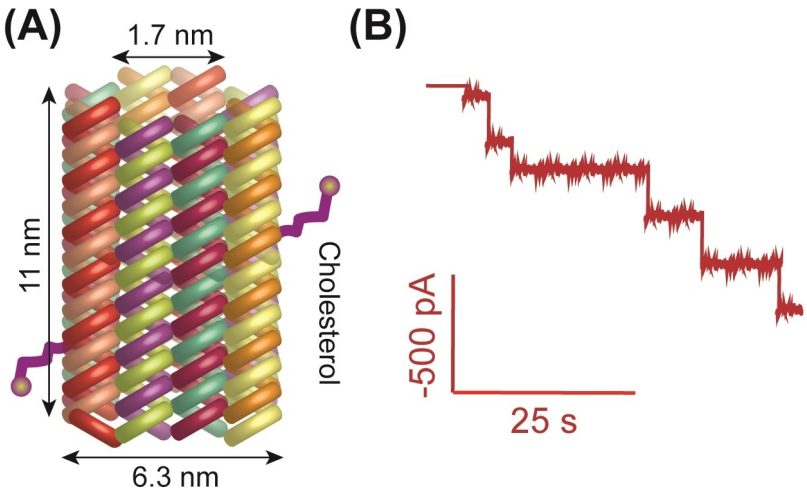

Figure 8. (A) Schematic design of the 11-nm tall, 6 RNA strands constructed RNA nanopore system having an inner diameter of 6.3 nm. The two cholesterol anchors are positioned on the sides of the nanopore (cholesterol, magenta); and (B) The corresponding single-channel bilayer recordings showing the characteristic step-wise insertions of the RNA nanopore in 1 M KCl, 5 mM HEPES (4-(2-hydroxyethyl)-1-piperazine ethane sulfonic acid), pH 8.0 under the applied transmembrane potential of −50 mV. Each step corresponds to ~150–200 pA. (A and B) Reproduced (modified) with permission from the corresponding author ref. 88. Figures were redrawn completely.

concentration; and (2) the rapid disintegration of its structural entities in biological media containing nucleases and other enzymes. Thus, the stability of DNA origami nanostructures under various biological components such as serum, growth media (e.g., Eagle's medium, Dulbecco's modified eagle medium (DMEM)), monovalent cations (Na^+, K^+) and divalent cations (Mg^{2+}, Ca^{2+}) constitutes an important parameter in several life-science applications. Howorka and his group used the same 6-HB[60] containing both cholesterol (NP-3 chol) and cholesterol devoid (NP-0 chol) structures to study the structural, functional, thermal stability and folding efficiency of DNA nanopores. The structures were found to be stable in buffers free from Mg^{2+} (NaCl, KCl, phosphate buffered saline, lysogeny broth, DMEM) and in lower level of Mg^{2+} solution. However, the structures did not migrate in the SDS-PAGE as protein-DNA aggregates occurred in samples containing fetal bovine serum (FBS) and DMEM medium. Additionally, except for FBS, the DNA nanopore remained water-soluble in all buffer systems after 2 days and subsequently bound to GUV's containing GFP. Thermal analysis through FRET-pair assays suggests that the structures exhibited high melting transitions above physiological temperatures (between 45° and 54 °C) in all the buffers free from Mg^{2+}.[89] Although the authors nanopore system is functionally stable in various tested buffers, these nanopores only appear to be stable for a few minutes in serum or protein-based buffer solutions, making sensing and other drug delivery assays extremely difficult.

4. Conclusions and future perspectives

DNA origami nanopores allow single-molecule sensing due to their intrinsic properties, such as label-free, amplification-free, and potentials for high-throughput screening. As described here in this review, the technique of DNA nanotechnology enables us to create DNA nanostructures of arbitrary shapes which is coupled with solid-state nanopores or serve as nanopore themselves. To date, two different forms of DNA origami nanopores have been reported (i) protein like DNA origami channels and (ii) hybrid DNA origami nanopores. The availability to fine-tune the pore diameter is a challenging issue in single-molecule sensing experiments which can be potentially overcome by DNA origami nanopores as one tune nanopores to precise molecular scales. Although the field of DNA nanotechnology has grown significantly in the last two decades, there are still many plethora of challenges, which are yet to be resolved. These include the degree of ion-current leakage that occurs through the walls of the origami channels on membrane bounding; gating effects that significantly disturbs the signal-to-noise ratio; channel closure/channel instability in response to high electric potential, aggregation of origami structures due to cholesterol or other hydrophobic modifications. Recent research suggests that a DNA duplex can also produce an ion current, further providing bilayer evidence for the ion-leakage nature of the DNA.[90]

Strategies including lowering the cholesterol anchors[91] or using alternate hydrophobic molecules such as porphyrin[69] or tocopherol linkers,[54] streptavidin-biotin attachment[54] and surfactants such as n-octyl-oligo-oxyethylene[89] were employed to debug the aggregation of DNA nanopores. However, lowering of the cholesterol anchors leads to a weaker interaction between the DNA structures and the hydrophobic lipid environment.[92] On the otherhand, surfactants cause the DNA structures to unfold in solution.[93] A much healthier approach was brought by Ohmann *et al.* by introducing ssDNA overhangs close to cholesterol anchors in small DNA constructs.[94] Nonetheless, the aggregation of larger DNA origami architects still depends on the number and position of the cholesterol anchors.

The platform of non-homogenous conductance is very often observed for DNA origami channels. It is likely that the higher channel conductance could be caused by the insertion of several agglomerated structures bound to the membrane. This is well corroborated with the TEM images where several structures bound to SUV's.[10,54] Well to less extent destabilized structures also prefer to insert, resulting in lower channel conductance than the theoretical prediction. Alternatively, these origami structures less often cause gating effects that interferes with the substrate permeation and data analysis. Although the stability issue was overcome by Burns *et al.*[89] it is still a topic of debate, when it comes to biological counterparts involving serum and other protein/nucleases.

To overcome the above obstacles, one can think of implementing new design strategies. For instance, the ion-current leakage in the DNA origami channels could be reduced by coating the structures with charged polymers[95,96]/polylysine[97]/protein(e.g., BSA)[98] or silica materials.[99] Such additional layers could result in rigid and stiffened structures, which causes less motion in the nanopore membrane. Additionally, it is expected that the structures can be stable for longer hours with less gating in response to high transmembrane potential, which is often the cause of DNA nanopore gating. These strategies have not been incorporated with existing DNA origami technologies, especially for nanopore measurements and this might open up new adventures and raise the competition with existing protein and solid-state nanopores in biosensing and other biotechnological applications.

Additionally, membrane bound DNA nano constructs are promising constituents for synthetic cell compartment or reaction networks. Chemical reactions and cascade mechanism occurring in biologically active cell could be replicated using membrane bound DNA nanoconstructs.[100] For instance, building giant networks of DNA nanostructures that could be linked with membrane-bound cell organelles for cell-cell communication, forms a high profile reaction cascade mechanism. No wonder, such transport process occurs in biology, for instance, networks that occur in cells through tunneling tubes,[101] where exchange/transport of organelles, ions, nucleic acid and other biological components occurs. Such a process plays a vital role in diseases such as cancer and other metabolic syndromes and mimicking such environment under *in vitro* conditions using synthetic DNA nanodevices could provide intriguing solutions in the near future.

Author's contributions

Conceptualization: Naresh Niranjan Dhanasekar. Writing original draft: Naresh Niranjan Dhanasekar. Figure preparation: Naresh Niranjan Dhanasekar, Durairaj Thiyagarajan. Reviewing and editing: Naresh Niranjan Dhanasekar, Dhiraj Bhatia.

Acknowledgements

The authors thank Dr. Arun Richard Chandrasekaran for his insightful comments in the preparation of this manuscript.

Conflict of Interest

The authors declare no potential conflict of interest is involved in the preparation of this manuscript.

Keywords: DNA origami · lipid bilayer · nanopores · biosensor · solid-state

[1] P. L. Yeagle, in The membranes of cells. Membrane transport. 3rd ed. P. L. Yeagle, Ed., Academic Press. Boston, MA, **2016**, 335 pp.
[2] D. Deamer, M. Akeson, D. Branton, *Nat. Biotechnol.* **2016**, *34*, 518–524.
[3] M. Wanunu, *Phys. Life Rev.* **2012**, *9*, 125–158.
[4] L. Restrepo-Pérez, G. Huang, P. R. Bohländer, N. Worp, R. Eelkema, G. Maglia, C. Joo, C Dekker, *ACS Nano* **2019**, *13*, 13668–13676.
[5] C. Cao, N. Cirauqui, M. J. Marcaida, E. Buglakova, A. Duperrex, A. Radenovic, M. Dal Peraro, *Nat. Commun.* **2019**, *10*, 4918.
[6] H. Brinkerhoff, A. S. W. Kang, J. Liu, A. Aksimentiev, C. Dekker, *Science* **2021**, eabl4381, doi: 10.1126/science.abl4381.
[7] K. Chuah, Y. Wu, S. R. C. Vivekchand, K. Gaus, P. J. Reece, A. P. Micolich, J. J. Gooding, *Nat. Commun.* **2019**, *10*, 2109.
[8] D.-H. Lee, S. Oh, K. L. B. Lee, G.-S. Yi, Y.-R. Kim, K.-B. Kim, C.-K. Lee, S.-W. Chi, M.-K. Lee, *Anal. Chem.* **2021**, *93*, 2811–2819.
[9] B. Sackmann, E. Neher, in Single-Channel Recording. 2nd ed. Kluwer Academic/Plenum, New York, **1995**.
[10] M. Langecker, V. Arnaut, T. G. Martin, L. List, S. Renner, M. Mayer, H. Dietz, F. C. Simmel, *Science* **2012**, *338*, 932–936.
[11] T. Diederichs, G. Pugh, A. Dorey, Y. Xing, J. R. Burns, Q. H. Nguyen, M. Tornow, R. Tampé, S. Howorka, *Nat. Commun.* **2019**, *10*, 5018.
[12] S. Zernia, N. J. van der Heide, N. S. Galenkamp, G. Gouridis, G. Maglia, *ACS Nano* **2020**, *14*, 2296–2307.
[13] T. Gutsmann, T. Heimburg, U. Keyser, K. R. Mahendran, M. Winterhalter, *Nat. Protoc.* **2015**, *10*, 188–198.
[14] N. Varongchayakul, J. Song, A. Meller, M. W. Grinstaff, *Chem. Soc. Rev.* **2018**, *47*, 8512–8524.
[15] J. J. Kasianowicz, E. Brandin, D. Branton, D. W. Deamer, *Proc. Natl. Acad. Sci. USA* **1996**, *93*, 13770–13773.
[16] M. Ayub, H. Bayley, *Curr. Opin. Chem. Biol.* **2016**, *34*, 117–126.
[17] Oxford Nanopore Technologies; Oxford Nanopore Technologies, **2020**. nanoporetech.com.
[18] F. Haque, J. Li, H.-C. Wu, X.-J. Liang, P. Guo, *Nano Today* **2013**, *8*, 56–74.
[19] C. Dekker, *Nat. Nanotechnol.* **2007**, *2*, 209–215.
[20] B. M. Venkatesan, R. Bashir, *Nat. Nanotechnol.* **2011**, *6*, 615–624.
[21] J. Li, D. Stein, C. McMullan, D. Branton, M. J. Aziz, J. A. Golovchenko, *Nature* **2001**, *412*, 166–169.
[22] H. Kwok, K. Briggs, V. Tabard-Cossa, *PLoS One* **2014**, *9*, e92880.
[23] B. Tu, S. Bai, B. Lu, Q. Fang, *Sci. Rep.* **2018**, *8*, 9097.
[24] E. C. Yusko, J. M. Johnson, S. Majd, P. Prangkio, R. C. Rollings, J. Li, J. Yang, M. Mayer, *Nat. Nanotechnol.* **2011**, *6*, 253–260.
[25] R. Brilmayer, C. Förster, L. Zhao, A. Andrieu-Brunsen, *Curr. Opin. Biotechnol.* **2020**, *63*, 200–209.
[26] L. J. Steinbock, O. Otto, C. Chimerel, J. Gornall, U. F. Keyser, *Nano Lett.* **2010**, *10*, 2493–2497.
[27] M. L. Kovarik, K. Zhou, S. C. Jacobson, *J. Phys. Chem. B* **2009**, *113*, 15960–15966.
[28] A. R. Hall, A. Scott, D. Rotem, K. K. Mehta, H. Bayley, C. Dekker, *Nat. Nanotechnol.* **2010**, *5*, 874–877.
[29] B. Cressiot, S. J. Greive, M. Mojtabavi, A. A. Antson, M. Wanunu, *Nat. Commun.* **2018**, *9*, 4652.
[30] N. C. Seeman, *J. Theor. Biol.* **1982**, *99*, 237–247.
[31] P. W. K. Rothemund, *Nature* **2009**, *440*, 297–302.
[32] K. Göpfrich, C.-Y. Li, M. Ricci, S. P. Bhamidimarri, J. Yoo, B. Gyenes, A. Ohmann, M. Winterhalter, U. F. Keyser, *ACS Nano* **2016**, *10*, 8207–8214.
[33] T. Diederichs, Q. H. Nguyen, M. Urban, R. Tampé, M. Tornow, *Nano Lett.* **2018**, *18*, 3901–3910.
[34] A. Gopinath, F. Miyazono, A. Faraon, P. W. K. Rothemund, *Nature* **2016**, *535*, 401–405.
[35] A. J. Thubager, W. Li, R. F. Johnson, Z. Chen, S. Doroudi, Y. L. Lee, G. Izatt, S. Wittman, N. Srinivas, D. Woods, E. Winfree, L. Qian, *Science* **2017**, *357*, eaan6558.
[36] Y. Amir, E. Ben-Ishay, D. Levner, S. Ittah, A. Abu-Horowitz, I. Bachelet, *Nat. Nanotechnol.* **2014**, *9*, 353–357.
[37] C. Zhou, X. Duan, N Liu, *Nat. Commun.* **2015**, *6*, 8102.
[38] M. Dai, R. Jungmann, P. Yin, *Nat. Nanotechnol.* **2016**, *11*, 798–807.
[39] T. Schlichthaerle, C. Lindner, R. Jungmann, *Nat. Commun.* **2021**, *12*, 2510.
[40] Q. Zhang, Q. Jiang, N. Li, L. Dai, Q. Liu, L. Song, J. Wang, Y. Li, J. Tian, B. Ding, Y. Du, *ACS Nano* **2014**, *8*, 6633–664.
[41] Z. Wang, L. Song, Q. Liu, R. Tian, Y. Shang, F. Liu, S. Liu, S. Zhao, Z. Han, J. Sun, Q. Jiang, B. Ding, *Angew. Chem. Int. Ed. Engl.* **2021**, *60*, 2594–2598.
[42] I. Mela, P. P. Vallejo-Ramirez, S. Makarchuk, G. Christie, D. Bailey, R. M. Henderson, H. Sugiyama, M. Endo, C. F. Kaminski, *Angew. Chem. Int. Ed. Engl.* **2020**, *59*, 12698–12702.
[43] D. Jiang, Z. Ge, H.-J. Im, C. G. England, D. Ni, J. Hou, L. Zhang, C. J. Kutyreff, Y. Yan, Y. Liu, S. Y. Cho, J. W. Engle, J. Shi, P. Huang, C. Fan, H. Yan, W. Cai, *Nat. Biomed. Eng.* **2018**, *2*, 865–877.
[44] P. Ketterer, A. N. Ananth, D. S. L. Trip, A. Mishra, E. Bertosin, M. Ganji, J. van der Torre, P. Onck, H. Dietz, C. Dekker, *Nat. Commun.* **2018**, *9*, 902.
[45] A. B. Farimani, P. Dibaeinia, N. R. Aluru, *ACS Appl. Mater. Interfaces* **2017**, *9*, 92–100.
[46] M. Raveendran, A. J. Lee, R. Sharma, C. Wälti, P. Actis, *Nat. Commun.* **2020**, *11*, 4384.
[47] H. Lee, A. K. R. Lytton-Jean, Y. Chen, K. T. Love, A. I. Park, E. D. Karagiannis, A. Sehgal, W. Querbes, C. S. Zurenko, M. Jayaraman, C. G. Peng, K. Charisse, A. Borodovsky, M. Manoharan, J. S. Donahoe, J. Truelove, M. Nahrendorf, R. Langer, D. G. Anderson, *Nat. Nanotechnol.* **2012**, *7*, 389–393.
[48] G. Zhu, J. Zheng, E. Song, M. Donovan, K. Zhang, C. Liu, W. Tan, *Proc. Natl. Acad. Sci. USA* **2013**, *110*, 7998–8003.
[49] D. Wang, Y. Fu, J. Yan, B. Zhao, B. Dai, J. Chao, H. Liu, D. He, Y. Zhang, C. Fan, S. Song, *Anal. Chem.* **2014**, *86*, 1932–1936.
[50] S. Surana, J. M. Bhat, S. P. Koushika, Y. Krishnan, *Nat. Commun.* **2011**, *2*.
[51] X. Li, Y. Li, L. Hong, *PLoS One* **2016**, *11*, e0162975.
[52] L. G. M. Ferrara, G. D. Wallat, L. Moynié, N. N. Dhanasekar, S. Aliouane, S. Acosta-Gutiérrez, J.-M. Pagès, J.-M. Bolla, M. Winterhalter, M. Ceccarelli, J. H. Naismith, *J. Mol. Biol.* **2016**, *428*, 4528–4543.
[53] E. Perozo, D. M. Cortes, P. Sompornpisut, A. Kloda, B. Martinac, *Nature* **2002**, *418*, 942–948.
[54] S. Krishnan, D. Ziegler, V. Arnaut, T. G. Martin, K. Kapsner, K. Henneberg, A. R. Bausch, H. Dietz, F. C. Simmel, *Nat. Commun.* **2016**, *7*, 12787.
[55] J. Yoo, A. Aksimentiev, *Proc. Natl. Acad. Sci. USA* **2013**, *110*, 20099–20104.
[56] A. Seifert, K. Göpfrich, J. R. Burns, N. Fertig, U. F. Keyser, S. Howorka, *ACS Nano* **2015**, *9*, 1117–1126.
[57] I. Bárcena-Uribarri, M. Thein, E. Maier, M. Bonde, S. Bergström, R. Benz, *PLoS One* **2013**, *8*, e78272.
[58] T. K. Rostovtseva, E. M. Nestorovich, S. M. Bezrukov, *Biophys. J.* **2002**, *82*, 160–169.
[59] V. Maingi, M. L. Lelimousin, S. Howorka, M. S. Sansom, *ACS Nano* **2015**, *9*, 11209–11217.
[60] J. R. Burns, A. Seifert, N. Fertig, S. Howorka, *Nat. Nanotechnol.* **2016**, *11*, 152–156.
[61] O. Mendoza, P. Calmet, I. Alves, S. Lecomte, M. Raoux, C. Cullin, J. Elezgara, *Nanoscale* **2017**, *9*, 9762–9769.
[62] D. Wang, Y. Zhang, M. Wang, Y. Dong, C. Zhou, M. A. Isbell, Z. Yang, H. Liu, D. Liu, *Nanoscale* **2016**, *8*, 3944–3948.

[63] R. P. Thomsen, M. G. Malle, A. H. Okholm, S. Krishnan, S. S.-R. Bohr, R. S. Sørensen, O. Ries, S. Vogel, F. C. Simmel, N. S. Hatzakis, J. Kjems, *Nat. Commun.* **2019**, *10*, 5655.
[64] S. Dey, A. Dorey, L. Abraham, Y. Xing, I. Zhang, F. Zhang, S. Howorka, H. Yan, *Nat. Commun.* **2022**, *13*, 2271.
[65] C. Lanphere, J. Ciccone, A. Dorey, N. Hagleitner-Ertuğrul, D. Knyazev, S. Haider, S. Howorka, *J. Am. Chem. Soc.* **2022**, *144*, 4333–4344.
[66] Y. Xing, A. Dorey, L. Jayasinghe, S. Howorka, *Nat. Nanotechnol.* **2022**, 17, 708–713.
[67] M. Debnath, S. Chakraborty, Y. P. Kumar, R. Chaudhuri, B. Jana, J. Dash, *Nat. Commun.* **2020**, *11*, 469.
[68] R. N. Das, Y. P. Kumar, O. M. Schütte, C. Steinem, J. Dash, *J. Am. Chem. Soc.* **2015**, *137*, 34–37.
[69] J. R. Burns, K. Göpfrich, J. W. Wood, V. V. Thacker, E. Stulz, U. F. Keyser, S. Howorka, *Angew. Chem. Int. Ed. Engl.* **2013**, *52*, 12069–12072.
[70] J. R. Burns, E. Stulz, S. Howorka, *Nano Lett.* **2013**, *13*, 2351–2356.
[71] J. R. Burns, N. Al-Juffali, S. M. Janes, S. Howorka, *Angew. Chem. Int. Ed. Engl.* **2014**, *53*, 12466–12470.
[72] J. Thiery, D. Keefe, S. Boulant, E. Boucrot, M. Walch, D. Martinvalet, I. S. Goping, R. C. Bleackley, T. Kirchhausen, J. Lieberman, *Nat. Immunol.* **2011**, *12*, 770–777.
[73] G. van der Goot, Pore-forming toxins, Springer, **2013**.
[74] J. Karolczak, D. Kowalska, A. Lukaszewicz, A. Maciejewski, R. P. Steer, *J. Phys. Chem. A* **2004**, *108*, 4570–4575.
[75] K. Göpfrich, C. Y. Li, I. Mames, S. P. Bhamidimarri, M. Ricci, J. Yoo, A. Mames, A. Ohmann, M. Winterhalter, E. Stulz, A. Aksimentiev, U. F. Keyser, *Nano Lett.* **2016**, *16*, 4665–4669.
[76] B. Hille, in Ion-channel of excitable membranes. 3rd ed. Sinauer Associates: Sunderland, MA, **2001**.
[77] J. Yoo, A. Aksimentiev, *J. Phys. Chem. Lett.* **2015**, *6*, 4680–4687.
[78] M. Raveendran, A. J. Lee, C. Wälti, P. Actis, *ChemElectroChem* **2018**, *5*, 3014–3020.
[79] S. Hernández-Ainsa, N. A. W. Bell, V. V. Thacker, K. Göpfrich, K. Misiunas, M. E. Fuentes-Perez, F. Moreno-Herrero, U. F. Keyser, *ACS Nano* **2013**, *7*, 6024–6030.
[80] Y. Youn, C. Lee, J. H. Kim, Y. W. Chang, D. Y. Kim, K. H. Yoo, *Anal. Chem.* **2016**, *88*, 688–694.
[81] S. Hernández-Ainsa, K. Misiunas, V. V. Thacker, E. A. Hemmig, U. F. Keyser, *Nano Lett.* **2014**, *14*, 1270–1274.
[82] C.-Y. Li, E. A. Hemmig, J. Kong, J. Yoo, S. Hernández-Ainsa, U. F. Keyser, A. Aksimentiev, *ACS Nano* **2015**, *9*, 1420–1433.
[83] E. A. Hemmig, C. Fitzgerald, C. Maffeo, L. Hecker, S. E. Ochmann, A. Aksimentiev, P. Tinnefeld, U. F. Keyser, *Nano Lett.* **2018**, *18*, 1962–1971.
[84] D. Ishikawa, Y. Suzuki, C. Kurokawa, M. Ohara, M. Tsuchiya, M. Morita, M. Yanagisawa, M. Endo, R. Kawano, M. Takinoue, *Angew. Chem. Int. Ed.* **2019**, *58*, 15299–15303; *Angew. Chem.* **2019**, *131*, 15443–15447.
[85] N. A. Bell, C. R. Engst, M. Ablay, G. Divitini, C. Ducati, T. Liedl, U. F. Keyser, *Nano Lett.* **2012**, *12*, 512–517.
[86] R. Wei, T. G. Martin, U. Rant, H. Dietz, *Angew. Chem. Int. Ed. Engl.* **2012**, *51*, 4864–4867.
[87] C. Plesa, A. N. Ananth, V. Linko, C. Gülcher, A. J. Katan, H. Dietz, C. Dekker, *ACS Nano* **2014**, *8*, 35–43.
[88] H. Li, S. Wang, Z. Ji, C. Xu, L. S. Shlyakhtenko, P. Guo, *Nano Res.* **2019**, *12*, 1952–1958.
[89] J. R. Burns, S. Howorka, *Nanomaterials* **2019**, *9*, 490.
[90] K. Göpfrich, T. Zettl, A. E. C. Meijering, S. Hernández-Ainsa, S. Kocabey, T. Liedl, U. F. Keyser, *Nano Lett.* **2015**, *15*, 3134–3138.
[91] A. Johnson-Buck, S. Jiang, H. Yan, N. G. Walter, *ACS Nano* **2014**, *8*, 5641–5649.
[92] S. Kocabey, S. S. Kempter, J. List, Y. Xing, W. Bae, D. Schiffels, W. M. Shih, F. C. Simmel, T. Liedl, *ACS Nano* **2015**, *9*, 3530–3539.
[93] J. List, M. Weber, F. C. Simmel, *Angew. Chem. Int. Ed. Engl.* **2014**, *53*, 4236–4239.
[94] A. Ohmann, K. Göpfrich, H. Joshi, R. F. Thompson, D. Sobota, N. A. Ranson, A. Aksimentiev, U. F. Keyser, *Nucleic Acids Res.* **2019**, *47*, 11441–11451.
[95] J. K. Kiviaho, V. Linko, A. Ora, T. Tiainen, E. Järvihaavisto, J. Mikkilä, H. Tenhu, Nonappa, M. A. Kostiainen, *Nanoscale* **2016**, *8*, 11674–11680.
[96] N. P. Agarwal, M. Matthies, F. N. Gür, K. Osada, T. L. Schmidt, *Angew. Chem. Int. Ed. Engl.* **2017**, *56*, 5460–5464.
[97] F. M. Anastassacos, Z. Zhao, Y. Zeng, W. M. Shih, *J. Am. Chem. Soc.* **2020**, *142*, 3311–3315.
[98] H. Auvinen, H. Zhang, Nonappa, A. Kopilow, E. H. Niemelä, S. Nummelin, A. Correia, H. A. Santos, V. Linko, M. A. Kostiainen, *Adv. Healthcare Mater.* **2017**, *6*, 1700692.
[99] X. Liu, F. Zhang, X. Jing, M. Pan, P. Liu, W. Li, B. Zhu, J. Li, H. Chen, L. Wang, J. Lin, Y. Liu, D. Zhao, H. Yan, C. Fan, *Nature* **2018**, *559*, 593–598.
[100] M. Langecker, V. Arnaut, J. List, F. C. Simmel, *Acc. Chem. Res.* **2014**, *47*, 1807–1815.
[101] R. Mittal, E. Karhu, J.-S. Wang, S. Delgado, R. Zukerman, J. Mittal, V. M. Jhaveri, *J. Cell. Physiol.* **2019**, *234*, 1130–1146.
[102] V. Maingi, J. R. Burns, J. J. Uusitalo, S. Howorka, S. J. Marrink, M. S. P. Sansom, *Nat. Commun.* **2017**, *8*, 14784.

Manuscript received: June 5, 2022
Revised manuscript received: August 7, 2022
Accepted manuscript online: August 10, 2022
Version of record online: August 24, 2022

Correction added on August 31 2022 after first online publication: Correction in author affiliations